2015

Dynamical systems analysis of electrostatic and aerodynamic forced vibrations of a thin flexible electrode

Sushma Bala Madanu
Iowa State University

Dynamical systems analysis of electrostatic and aerodynamic forced vibrations of a thin flexible electrode

by

Sushma Bala Madanu

A thesis submitted to the graduate faculty

in partial fulfillment of the requirements for the degree of

MASTER OF SCIENCE

Major: Engineering Mechanics

Program of Study Committee:
Thomas Ward III, Major Professor
Christina Lynne Bloebaum
Hui Hu

Iowa State University

Ames, Iowa

2015

DEDICATION

I dedicate this work to God and my family members who supported me with love, comfort and prayers when I am thousands of miles away.

TABLE OF CONTENTS

Page

LIST OF FIGURES

LIST OF TABLES

ACKNOWLEDGEMENTS

I would like to express my honest gratitude to Dr. Thomas Ward for his patient guidance, encouragement and valuable suggestions of this research for a first time researcher like me and for his support for my graduate studies and in the class Incompressible flow aerodynamics; without him these would not have been possible. I would like to thank Stanley I. Barbel for his assistance in conducting the research and Andrew R. White for all his help in academics and research throughout my master's program. I would like to thank Cory D. Hinton for laying the foundation for this research. I am very thankful to Dr. Christina L. Bloebaum for her guidance in the class Multi-disciplinary optimization and for serving on my program of study committee. I would also like to thank Dr. Hui Hu for his assistance in serving as a member of my committee. Finally, I would like to thank the Department of Aerospace Engineering at Iowa State University for equipping me with greater knowledge and support to pursue master's here.

ABSTRACT

Transverse vibrations of an electrostatically actuated thin flexible cantilever perturbed by low-speed air flow is studied using both experiments and numerical modeling. In the experiments the dynamic characteristics of the cantilever are studied by supplying a DC voltage with an AC component for electrostatic forcing and a constant uniform air flow around the cantilever system for aerodynamic forcing. The maximum voltage applied varies from 1 – 9 kV and air flow speeds range from 0.224 – 3.58 m/s (0.5 – 8 mile/hr). The Reynolds numbers for these speeds lie in the range of $10^3 - 2 \times 10^4$. A range of control parameters leading to stable vibrations are established using the Strouhal number as the operating parameter whose inverse values change from $100 - 2500$. The Numerical results are validated with experimental results. Assuming the amplitude of vibrations are small, then a non-linear dynamic Euler-Bernoulli beam equation with viscous damping and gravitational effects is used to model the vibrations of the dynamical system. Aerodynamic forcing is modelled as a temporally sinusoidal and uniform force acting perpendicular to the beam length. The forcing amplitude is found to be proportional to square of air flow velocity by obtaining relationship between the experimental amplitude of vibrations and air flow velocity. Numerical results strongly agree with those of experiments predicting accurate vibration amplitudes, displacement frequency and quasi-periodic displacements of the cantilever tip.

CHAPTER 1. INTRODUCTION

Development of micro air vehicles (MAVs) has spawned interest in using mechanical flapping wing for flight in opposition to the conventional artificial flying members that use fixed wing for flying. This interest aroused from the explanations of biologists and naturalists that continuously flapping natural fliers (insects and birds) whose size is similar to MAVs fall in low-Reynolds number regime of 10^2-10^5 where the flow field is unsteady, laminar and incompressible [1, 2] (see Figure 1.1) and due to the already available defined configurations, kinematics and aerodynamics of flapping flight of natural fliers determining wing span, material and design [3]; forward velocity, acceleration [4]; power required [5]; aerodynamics [5, 6], body size, wing beat time [7]; suitable air flow speeds and their aerodynamics [8, 5, 9] and mechanisms and maneuverability[10].

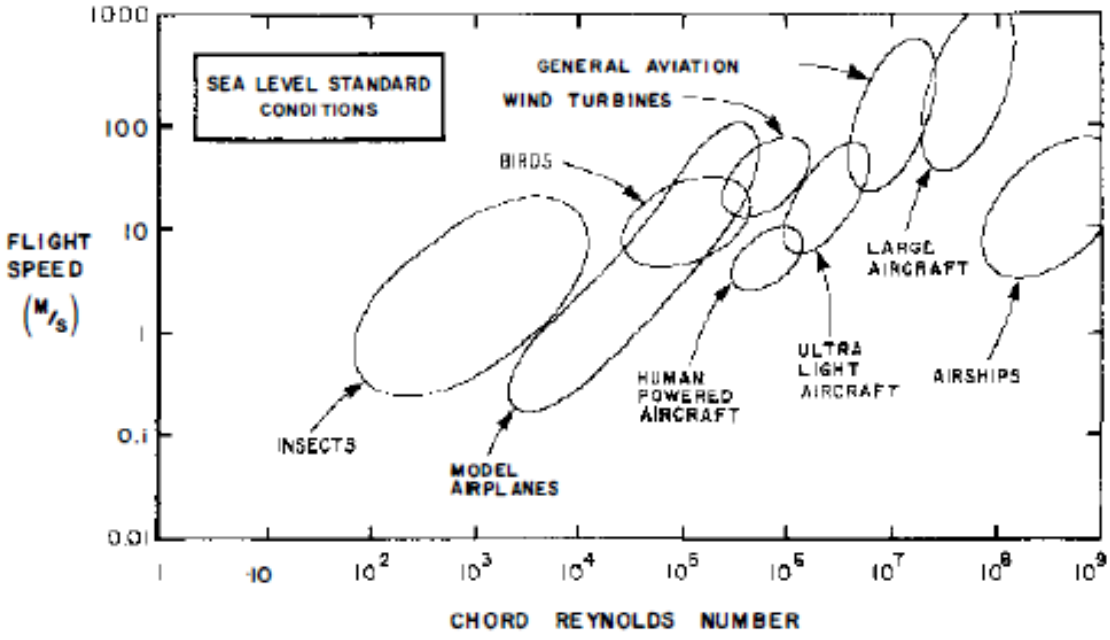

Figure 1.1: Reynolds number regime for natural and artificial fliers [P. B. S. Lissaman].

Although, flapping wing motion cycle is complex including flexing, twisting, rotating or feathering of wings [11], in the development process of artificial fliers, most researchers concentrated on this motion because studies show millions of biological flying species use it as the transportation mode and also demonstrated improved performance in the low speed air flow conditions [12]. Therefore in this study we want to model this flapping coupled with aerodynamic forces as a dynamical system similar to damped forced pendulum with quasi-periodic forcing [13] to develop control strategies suitable for controlled flying. There are only few MAVs (insect and bird sized) which demonstrated flight in low speed air environments [14, 15, 16].

The only successful flying MAV by flapping motion of wings closely resembling bird size is Nano Hummingbird (see Figure 1.2) developed by AeroVironment[16]. We are inspired by this nano hummingbird which uses flexible membrane for flapping wings whose length is 7.4 cm and mass is 0.26 g spanning 16.5 cm, flaps at 30 Hz flap rate and flies at a speed of 6.7 m/s weighing 19 g. The flapping mechanism used is a string based mechanism and a hybrid control mechanism, servo motors combined with geartrain is used for control of flapping under aerodynamic loads.

In this study reduced order model of Nano hummingbird is studied to develop the dynamical system. For the experimental purposes, non-lifting case is considered and the flapping is restricted to one degree of freedom i.e. only transverse displacement occurs with no twisting or rotation. The wing is designed as a simple rectangular flexible cantilever of length ≈ 7 cm and flapping is generated with limited kinematics by electrostatic actuation with sinusoidal and non-sinusoidal input signals at frequencies ranging from 1-8 Hz.

Figure 1.2: Nano Hummingbird [M. Keennon et al.].

Electrostatic actuation is deflection of movable electrode closer to ground electrode upon application of potential difference between the electrodes. This motion occurs due to the charge build-up on conducting surfaces which gives rise to attracting electric field as explained in [17, 18]. Microelectromechanical systems (MEMS) for many years now are extensively using this actuation for manufacturing sensors, transducers and resonators using silicon and polymer based substrates due to its very good performance in achieving repeated motion quickly when forced periodic loading is applied. Therefore we would like to take advantage of this feature with macro-scale conducting flexible cantilever beam. Figure 1.3 shows single cantilever MEMS sensor used in scanning probe microscopy [19].

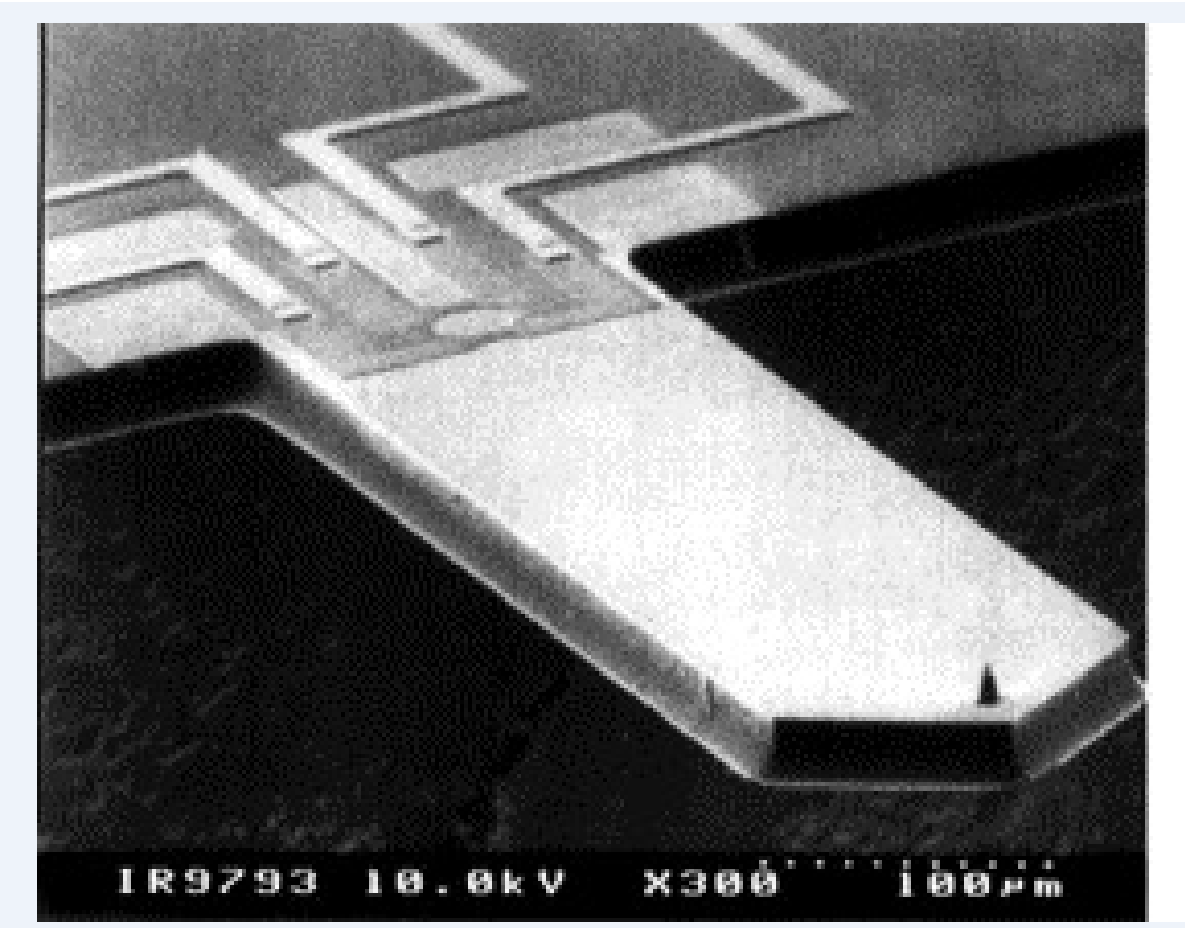

Figure 1.3: Single cantilever MEMS sensor [T. Gotszalk et al.].

1.1 Literature Review

Mimicking flapping wing flight of natural fliers for propulsion of artificial fliers, MAVs is interesting to researchers, government organizations and military since several years due to their applications in search and rescue operations, surveillance and targeting. For the search and rescue operations in earthquake debris and fire-explosions in buildings we need to have controlled flying vehicles in lower air flow speed environments whose size is small and is reliable and for surveillance and targeting the enemy through spying operations these vehicles should satisfy controlled flying in low speed air flow environments resembling natural fliers.

Given these constraints, the vehicles are being developed utilizing the studies of natural fliers made by biologists.

Based on these studies, MAVs configurations for flapping are established. Spedding et al. [20] showed that the wingspan is between 10-20 cm, Mueller [21] studied aerodynamics and performance of airfoil geometries for MAVs and Madangopal et al. [22] studied energy storage mechanism and aerodynamic wing models for MAVs. Control of flapping for obtaining successful flight is the main issue. Considering a rigid wing the flapping kinematics are developed using 2 DOF four bar linkage mechanism, carefully designing the wings for minimized flexure stresses. The aerodynamic force experienced by the wing is measured using strain gages mounted on its tip and second order ordinary differential equation (ODE) for motion of the tip with stiffness of spar and damping of wing is developed accounting for this force [23] for closed loop control signals. Later 3 DOF four bar linkage mechanism kinematics of flapping is studied using energy methods. Smith studied unsteady aerodynamics of tethered moth's flapping wings using panel method [24]. He concluded that including wake in the analyses of the unsteady aerodynamics of flexible wings undergoing arbitrary, large-scale motion leads to the control of resultant aerodynamic force. Later on the kinematics for flapping were designed similar to those of hummingbird with ball-and-socket joint at the shoulder and simulated to produce the same wing beat patterns. A feedback control circuit inspired by locust morphology was developed to automatically tune the actuator drive signal to the resonant flapping frequency of the flexible wing structure. The strain-rate sensor attached to the wing gives positive rate feedback to the circuit for its control [25]. This generated wing beat patterns that approximately matched those of hummingbird's flight.

However the equation of motion for flapping, developing suitable aerodynamic model is not yet studied for macro-scale (centimeter scale) flapping flexible wings. The motivation for this study is to better understand the continuous control of flapping mechanical systems

in low speed wind gusts [16, 26, 27]. This development would prove useful for control of flapping. This can be studied by observing flapping generated by simple kinematics. Simple kinematics leading to flapping is observed in vibration of cantilever beams actuated by electrostatic forcing in the MEMS technology. The electrostatic force is produced by supplying DC voltage with small AC component. These cantilevers undergo small deflections whose dynamic characteristics can be studied using Euler-Bernoulli beam theory [28, 29, 30]. The deflections are stable only if the voltage applied for actuation is below pull-in voltage for a given gap distance between the electrodes [31, 32, 33, 34]. [35] studied this actuation for generating the vibrations of macro-scale cantilever beam quantifying for influence of voltage, frequency and input signal type for two different gap distances. He concluded that the system's behavior is stable for linear input signal at natural frequency of the beam. He proposes to test the system in wind gusts to study the controllability of this actuation. The study of electrostatically actuated MEMS has been extended to observing dynamic characteristics of the beams submerged in fluid media [28, 36] for better control of deflection amplitudes. The force due to the fluid-loading was modelled as added mass. Thus inertial and conductivity effects of surrounding fluid is studied. If the fluid will be constantly flowing around the cantilever system i.e. it is not stationary, then there is a need to model the aerodynamic load acting on the beam. But this case is quite common in development of MAVs which requires significant research to analyze the control parameters. [37] has studied the effect of surrounding stationary air damping on free vibrations of cantilever beam. This is modelled as air damping due to drag force proportional to velocity of vibration for small amplitudes and proportional to dynamic pressure for large amplitudes. The forced vibration analysis of cantilever beams due to two types of forcing, mechanism generating flapping and aerodynamic forcing can be viewed as multiple forced damped pendulum [13, 38, 39, 40] or extension of single periodic forcing to multiple periodic forcing for explaining dynamical systems with two forcing [41]. Studying these systems could lead to better understanding of controlling the vibrations.

1.2 Current Research

In this manuscript we present experimental and computational data for the electrostatic and aerodynamic forcing of a flexible electrode cantilever beam. The purpose is to study the range of parameters for which periodic electrostatic forcing of a flexible electrode cantilever [30, 28, 31, 35, 42, 43] can be used to control the beam vibrations in the presence of a non-lifting aerodynamic load. The flexible electrode in this study is a plastic substrate with one side containing a nanometer thin coating of metal. The thin metal coating does not hinder flexing of the plastic such that it can be considered a homogeneous material with a constant and uniform elastic modulus, E. With this understanding we develop mathematical expressions based on the Euler-Bernoulli beam theory to study the dynamics of both, electrostatic and aerodynamic forcing of the flexible cantilever electrode. Here we are interested in developing robust reduced order models so that they may be used as a test bed for understanding control of dynamic behavior that arises in these types of complex systems [44, 45, 46, 47].

To develop a model for the dynamical systems that arises from the coupled forced vibrations of a flexible electrode cantilever we consider the Euler-Bernoulli beam theory. The Euler-Bernoulli beam theory is analogous to the classic forced pendulum with damping [13, 38, 40, 48, 49]. The two systems can be made similar by replacing gradient in the shear force from the Euler-Bernoulli beam theory with the linear displacement term from Hooke's law. For the classic forced pendulum with damping a harmonic oscillator is subjected to both damping that is proportional to the velocity, and a sinusoidal perturbation that contains both an amplitude and frequency. For certain values of the parameters used to represent the damping coefficient, and forcing amplitude and frequency, the pendulum is known to exhibit chaotic behavior as measured by Poincaré mapping [13, 38] among other methods. Here we model the coupled forced vibrations of a flexible electrode cantilever beam

using Euler-Bernoulli beam theory with a viscous damping term that is proportional to the velocity [28, 50], although other models exists which utilize higher order derivatives [49]. The forcing terms consist of a fully non-linear electrostatic term [30, 28] and a periodic aerodynamic forcing term based on a drag force, F_D [37]. The aerodynamic forcing results in small amplitude displacements so that the Euler-Bernoulli theory may be applied, and also allows us to neglect any lifting forces [37].

While the dynamical system may be analogous to the forced pendulum leading to periodic or chaotic motion depending on the input parameters, it is not necessarily the only source of complex behavior. Since both forcing mechanisms are periodic then other explanations for complex motion may exist. In the literature it has been shown that the summation of two harmonic forcing terms is also known to produce *random* behavior although it is typically not characterized as chaotic and instead is considered quasi-periodic as determined by the multiple forced pendulum [40]. We will use the experiments and numerical model to determine the source for any random behavior based on these two (chaotic and quasi-periodic) possible explanations from the dynamical systems literature.

The phase plane diagrams obtained from experimental and numerical data show chaotic results at higher air flow speeds and could not be compared to draw conclusions about the system's behaviour. Therefore a dimensionless parameter, the Strouhal number,

$$St = \frac{u_{L,e}\omega_\phi}{U_\infty} \tag{1.1}$$

is used to characterize the vibrational response to the coupled forcing [51, 52, 53, 54]. For this study it is defined the ratio of the vertical velocity of the flexible electrode tip due to electrostatic forcing $u_{L,e}\omega_\phi$ to the axially imposed free stream velocity, U_∞. Note that in this definition of the Strouhal number the two velocities are perpendicular. The displacement frequencies due to aerodynamic forcing always occur at values close to the flexible electrode

cantilever's natural frequency ω_n. Therefore, for the electrostatic forcing we use subharmonic frequencies ω_ϕ for comparison with the cantilever tips frequency response as a function of St.

In the next chapter we describe the mathematical model for the vibrating cantilever beam that is based on the Euler-Bernoulli beam theory. This chapter includes a non-dimensionalization of the equation which reveals a set of dimensionless parameters that are used to characterize the system. In the chapter that follows we describe the experimental setup and procedure. This chapter includes some characterization of the electrostatic properties of the beam and range of air flow speeds. Results of the experiments and computation are presented in the next chapter. These are followed by some detailed discussion of the comparison and then followed by concluding remarks.

CHAPTER 2. GOVERNING EQUATIONS

Consider a flexible cantilever beam made of a semi-rigid plastic material coated with a thin (nanometer scale) metal film on one side with elastic modulus E, density ρ and mass m. The thin flexible cantilever extends out from an insulated post with length L and width b such that $b/L \ll 1$ whose cross-sectional area is A. Gravitational forces cause deformation of the cantilever in the absence of any external forcing. Therefore, the cantilever is separated from a ground electrode by a non-uniform distance a. The cantilever is subjected to distributed dynamic loads resulting in small transverse vibrations. We are interested in dynamic loads that are applied electrostatically due to a combination of a DC voltage ϕ_1 and an AC voltage ϕ_2 by $\phi(t) = \phi_1 + \phi_2\Lambda(2\pi\omega_\phi, t)$ where the AC component is generated by a periodic signal, Λ assuming that electric field intensity is independent of width and no fringing fields are formed due to the insulating surfaces on other side of electrodes. We are also interested in aerodynamic forcing due to a uniform flow of air at constant speed, U_∞. The orientation of the cantilever beam relative to the loads are such that the electrostatic forcing is lateral and the aerodynamic forcing is axial. Figure 2.1 shows a schematic of the problem proposed in this study where the beam is positioned with its length along the x-axis separated from the ground electrode with non-uniform gap distance, a.

Both forms of dynamic forcing cause transverse vibrations i.e. displacement due to forcing occurs in the y-direction for the cantilever beam. The displacement of the beam is represented by $u(x,t)$ and is an aggregate of displacements due to electrostatic forcing $u_e(x,t)$, aerodynamic forcing $u_a(x,t)$ and gravity $u_g(x)$. The maximum amplitude of the cantilever beam vibrations occur at the free end of the beam, $u_L = u(L,t)$, for the range of parameters studied here. The equation of motion governing the proposed cantilever beam

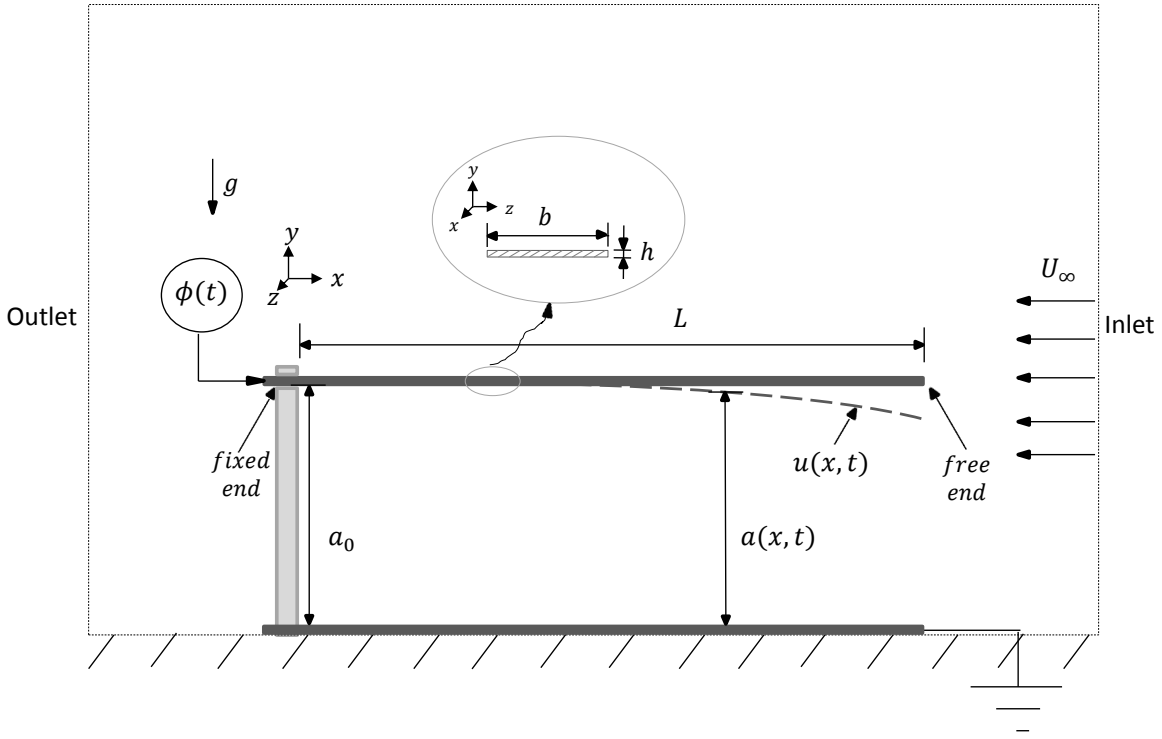

Figure 2.1: Schematic of deflection of the beam due to electrostatic, aerodynamic and gravitational loads.

system is developed using the Euler-Bernoulli beam theory with forcing terms for electrostatic forcing presented in [30, 28, 35] and the expression for aerodynamic forcing is developed by examining experimental results. It is observed that for small constant aerodynamic loads applied on the beam, it vibrates at its natural frequency ω_n with amplitudes suitable for small deflection analysis. The displacement though is non-uniform for all substantial displacements resulting in seemingly random motion that may represent a chaotic system. This effect can be taken into account by modelling the aerodynamic forcing as uniform sinusoidal forcing, perpendicular to the beam length whose amplitude is k N/m. This k value varies for aerodynamic forcing and combined electrostatic and aerodynamic forcing cases. Besides these external forces, the surrounding air has damping effects on this vibrating cantilever whose distributed viscous damping coefficient is μ. The governing equation of motion for the transverse vibrations of the beam is

$$\rho A\frac{\partial^2 u}{\partial t^2}+\mu\frac{\partial u}{\partial t}+EI\frac{\partial^4 u}{\partial x^4}=-\frac{\epsilon_0\epsilon_v b}{2}\left(\frac{\phi(t)}{a_0+u}\right)^2+k\sin(2\pi\omega_n t)-\frac{mg}{L} \tag{2.1}$$

where the terms on left hand side are inertial force, viscous damping force and internal restoring force respectively and forcing terms on right hand side are electrostatic, aerodynamic and a constant gravitational load, respectively in which I is the second moment of area of cantilever, ϵ_0 and ϵ_v are relative permittivity of air and permittivity of vacuum respectively, g is gravitational acceleration constant and t is the time of oscillations. We are neglecting any dynamic damping so the actual beam velocity due to displacement is relatively small. The periodic forcing expression is $\phi(t)=\phi_1+\phi_2\Lambda(2\pi\omega_\phi,t)$ where the function $\Lambda(2\pi\omega_\phi,t)$ is sine, square or triangle waveform and the total voltage applied is $\phi_{max}=\phi_1+\phi_2$. Vibrations due to a particular forcing can be found by equating the other right hand side forcing terms to zero.

The dimensional amplitude of vibration at the free end of the beam after subtracting the gravitational deflection $u_g(x)$, i.e. displacements due to combined electrostatic and aerodynamic loads is represented by $u_{L,e+a}$. Separately the electrostatic and aerodynamic load are represented by $u_{L,e}$ and $u_{L,a}$, respectively. Below we describe the dimensionless equation of motion for the cases of only electrostatic forcing with gravity and the unsteady linear equations. Solutions to these two additional forms of the equation of motion are used to compare with experimental data in order to estimate the elastic modulus and damping coefficient, respectively.

2.1 Numerical Analysis: Non-Dimensionalization

For numerical analysis the equations of motion are made dimensionless by scaling lengths with the non-deformed beam length L and time with an initially unknown variable $1/\Omega$ in 1/Hz. The mathematical expression for Ω is obtained by non-dimensionalizing Eq.

2.1. Therefore, the dimensionless independent and dependent variables are $u^* = \frac{u}{L}$, $x^* = \frac{x}{L}$ and $t^* = t\Omega$ and the dimensionless form of Eq. 2.1 is

$$\frac{\partial^2 u^*}{\partial t^{2*}} + \Pi_\mu \frac{\partial u^*}{\partial t^*} + \frac{\partial^4 u^*}{\partial x^{4*}} = \frac{-\Pi_e}{(1 + R^* u^*)^2} f^2(2\pi\omega_\phi t) + \Pi_a \sin(2\pi\omega_n t) - \Pi_g \tag{2.2}$$

where

$$\Pi_\mu = \frac{\mu}{\rho A \Omega} \tag{2.3a}$$

$$\Pi_e = \frac{b\epsilon_0\epsilon_v\phi_{max}^2}{2m(a_0\Omega)^2} \tag{2.3b}$$

$$\Pi_a = \frac{k}{m\Omega^2} \tag{2.3c}$$

$$\Pi_g = \frac{g}{L\Omega^2}. \tag{2.3d}$$

The other variables that appear are $\mu = C/L$ and $R^* = L/a_0$ in which C is viscous damping coefficient and a_0 is distance between electrodes at $x = 0$. With the scaling used here the inverse time scale is proportional to the undamped natural frequency $\Omega = \sqrt{EI/(mL^3)}$. The transient electrostatic forcing term is now $f(2\pi\omega_\phi t) = \phi(t)/\phi_{max}$. Also note that the mass can be replaced by the beam density and dimensions using $m = \rho AL$.

Boundary conditions for the cantilever beam at $x^* = 0$ are,

$$u^*(0, t^*) = 0 \tag{2.4a}$$

$$\left.\frac{\partial u^*}{\partial x^*}\right|_{x^*=0} = 0 \tag{2.4b}$$

and

$$\left.\frac{\partial^2 u^*}{\partial x^{2*}}\right|_{x^*=1} = 0 \tag{2.5a}$$

$$\left.\frac{\partial^3 u^*}{\partial x^{3*}}\right|_{x^*=1} = 0 \tag{2.5b}$$

at the free end $x^* = 1$. These are the typical boundary conditions for the Euler-Bernoulli beam problem which represent a fixed end and symmetry at $x^* = 0$ and zero curvature and gradient in the curvature at $x^* = 1$.

The beam is initially displaced due to gravity with a zero velocity resulting in the initial conditions,

$$u^*(x^*, 0) = -\frac{\Pi_g}{24}(x^{4*} - 4x^{3*} + 6x^{2*}) \tag{2.6a}$$

$$\left.\frac{\partial u^*}{\partial t^*}\right|_{t^*=0} = 0. \tag{2.6b}$$

The equations are solved using 4^{th} order accurate finite difference discretization of the spatial derivatives. The 4^{th} order scheme is also applied to the boundary conditions. The equations are advanced in time using an adaptive 4^{th} order accurate Runge-Kutta-Merson (RKM) adaptive time stepping algorithm. With the RKM method it is possible to estimate the truncation errors and modify the time step accordingly to achieve a given precision [55].

2.2 Steady Non-Linear Euler-Bernoulli Beam Equation

The steady form of Eq. 2.2 with $\Pi_\mu = \Pi_a = 0$, $\phi(t) = \phi_{max}$ and zero acceleration describes displacements due to DC electrostatic forcing. The steady equation is used to

estimate the elastic modulus of the beam by comparing numerical and experimental data for the maximum cantilever displacement. The maximum displacement is determined by the non-linear ordinary differential equation

$$\frac{d^4u^*}{dx^{4*}} = -\left[\frac{\Pi_e}{(1+R^*u^*)^2} + \Pi_g\right]. \tag{2.7}$$

The maximum amplitude of deflection occurs at the free end of the beam due to electrical forcing which is denoted by $u^*_{L,e}$. If the maximum deflection is very small such that $R^*u^* \ll 1$ then the problem reduces to linear static equation of deflection $d^4u^*/dx^{4*} = -(\Pi_e + \Pi_g)$ with the solution written as $u^*(x^*) = -(\Pi_e + \Pi_g)/24[x^{4*} - 4x^{3*} + 6x^{2*}]$.

However, if the displacement is *relatively* large such that $R^*u^* \not< 1$ then the non-linear equation must be solved in order to use it to estimate the elastic modulus. Solutions of the non-linear ODE problem are non-trivial since only two boundary conditions are applied at $x^* = 0$ based on Eqs. 2.4 and 2.5. Therefore, there is no means of solving the equation by using strictly explicit methods. To solve the non-linear ODE equation we will apply a double shooting method for the two boundary conditions given by Eq. 2.5.

The initial *guesses* used to initiate the shooting method are based on solutions to the linear static Euler-Bernoulli beam equation. For small values of R^* the values of the boundary conditions should be in the vicinity of those given by the linear solution. Using these as initial guesses it is possible to build an algorithm that iterates to find the correct boundary conditions using,

$$\left[\frac{d^2u^*}{dx^{2*}}\Big|_{x^*=0}\right]_n = -(1+C_{1n})\left(\frac{\Pi_e + \Pi_g}{2}\right) \tag{2.8a}$$

$$\left[\frac{d^3u^*}{dx^{3*}}\Big|_{x^*=0}\right]_m = (1+C_{2m})(\Pi_e + \Pi_g). \tag{2.8b}$$

The iteration step is denoted using n and m. The constants C_{1n} and C_{2m} are varied to produce boundary condition estimates that are in the range given by the linear solution. Initially a large range of values are chosen for the constants. After the first set of iterations then a second range of values for the two constants are determined based on values that overlap and contain a minimum in the values at $x^* = 1$. The range of values is checked to determine where the values overlap after each set of iterations until the range of value narrows until an approximate local minimum is found where the boundary conditions at $x^* = 1$ are satisfied. The errors associated with the approximation of the minimum can be determined by the size of the final range of values for the two constants and the associated solutions to the ODE. So when reporting solutions to the ODE the displacement obtained from all the iterations in the final range of values are averaged.

2.3 Unsteady Linear Euler-Bernoulli Beam Equation

The unsteady Euler-Bernoulli beam equations can be used to estimate the unknown damping coefficient C. We are assuming that the damping coefficient is independent of any external forcing and does not vary with time. To estimate the coefficient we keep in mind that any displacement of the beam from its initial position due to gravitational forces should result in an underdamped system. Then we can estimate the damping coefficient by comparing the transient maximum displacement of the cantilever beam denoted by $u_{L,0}$ between numerical data for a given value of C and the experimental data with the same initial conditions.

The equation governing an underdamped cantilever beam is given by

$$\frac{\partial^2 u^*}{\partial t^{2*}} + \Pi_\mu \frac{\partial u^*}{\partial t^*} + \frac{\partial^4 u^*}{\partial x^{4*}} = -\Pi_g \tag{2.9}$$

where we have set $\Pi_e = \Pi_a = 0$ in Eq. 2.2. Under these conditions it is possible to generate an underdamped displacement using the initial condition

$$u^*(x^*, 0) = 0 \tag{2.10a}$$

$$\frac{\partial u^*}{\partial t^*}\Big|_{t^*=0} = 0. \tag{2.10b}$$

The equations are solved using 4^{th} order finite difference discretization in space and the RKM method with 4^{th} order accuracy in time.

CHAPTER 3. EXPERIMENTS

3.1 Experimental Setup and Materials

The experimental setup is similar to a parallel plate capacitor with an electrode rigidly fixed at one end using a tapped cylindrical acrylic post and an insulated bolt with the dielectric medium being ambient air shown as electrostatic actuation setup (see Figure 3.1). This system is enclosed in an open circuit wind tunnel, by sliding the acrylic post through a hole drilled into the bottom acrylic plate of the wind tunnel. The wind tunnel is an acrylic box that is built by bolting four 0.3 x 0.3 x 0.013 m^3 acrylic plates whose leading edges are attached with semi-circular acrylic strips for smooth flow. The diameter of the hole is equal to the outer diameter of the acrylic post. The length of the acrylic post is selected such that the distance between the electrodes can be adjusted according to the experimental requirements. The beam is a $\approx$ 70 x 13 x 0.2 mm^3 polyester film (Delta Technologies Limited) coated with thin layer of metals $In_2O_3/Au/Ag$ on the side facing fixed electrode at some distance. The fixed electrode is designed by gluing a larger PET film (150 x 150 x 0.2 mm^3) with a hole, on the inside face of the bottom plate of the wind tunnel such that the hole aligns with that in the plate. The whole system rests on metal risers to adjust the gap distance between the electrodes. Parameters of the beam and the dielectric medium are defined in Table 3.1.

A signal generator (Agilent Technologies) in series with a high voltage amplifier (Spellman) supplies the DC/AC voltage at very low currents of milli-ampere scale with a certain input signal and frequency. Voltage was supplied through the supply wire to the fixed end of the flexible electrode while fixed electrode is grounded by ground wire. The voltage supplied

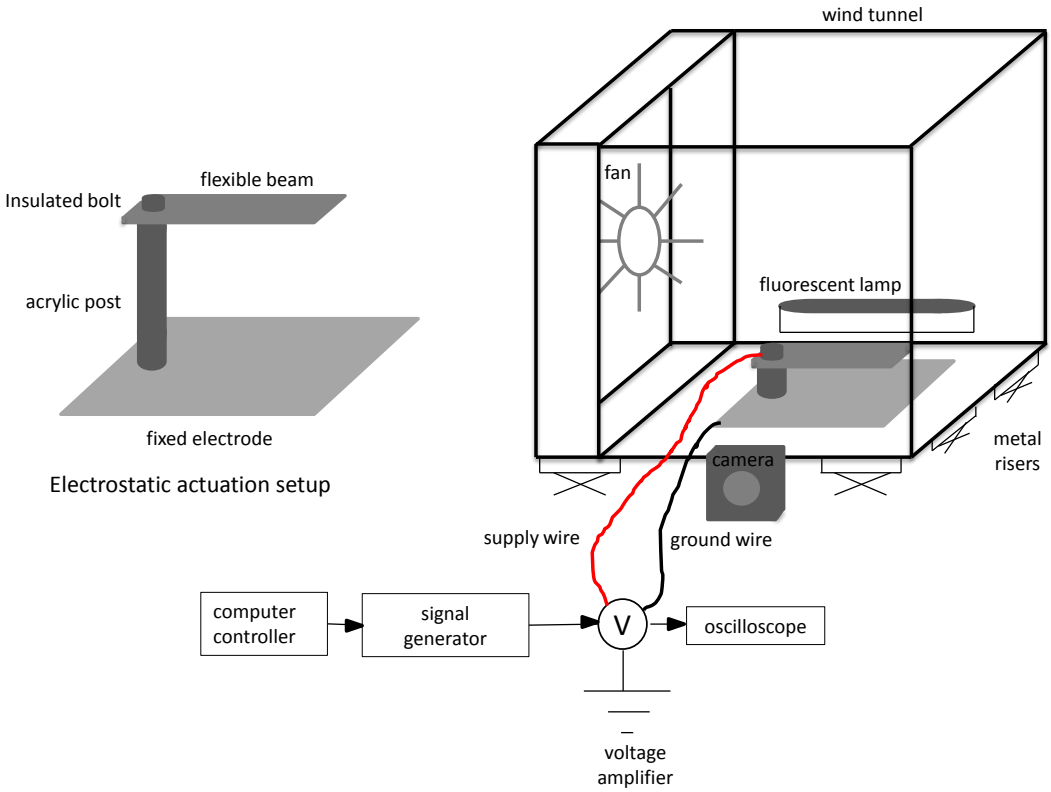

Figure 3.1: Experimental setup showing system for testing electrostatic vibrations subjected to wind gusts in the wind tunnel.

Table 3.1: Parameters of the beam and the dielectric medium

Parameter	Value
Cross-sectional area, A	2.6 mm^2
Area moment of inertia, I	0.0087 mm^4
Modulus of elasticity, E	3.1 GPa
Density, ρ	1185 kg/m^3
Mass, m	251 mg
Vacuum permittivity, ϵ_v	8.854x10^{-12} F/m
Relative permittivity of air, ϵ_0	1

includes the DC input ϕ_1 and AC modulation amplitude ϕ_2 where the DC component is the offset and AC component is the amplitude of modulation in the waveform generator. These values are determined using an oscilloscope whose ranges are $0.5 < \phi_1 < 6.5$ kV,

$0.5 < \phi_2 < 2.5$ kV and ratio ϕ_1/ϕ_2 is equal to 1 at 1 Hz and increases by $\approx 25\%$ as the frequency increases. A small box fan (Pentair) draws air at different speeds using voltage regulator (Staco Energy) through the wind tunnel inlet past the system giving rise to aerodynamic perturbations. The vibrations occur perpendicular to the beam length i.e., in the plane of beam thickness.

These beam vibrations in the plane of beam thickness are captured by cameras. These are placed such that the side view of the experimental setup (which is the plane of vibrations) at the beam tip can be captured. A CCD slow camera (Pixelink) records videos at 250 frames per second in a 200 x 200 pixels window with a resolution of beam thickness, h = 0.2 mm = 24 pixels or 120 pixels = 1 mm (see Figure 3.2) for smaller vibration amplitudes and a fast camera (Hotshot) records videos at 1000 frames per second in a 500 x 200 pixels window with a resolution of h = 26 pixels or 130 pixels = 1 mm (see Figure 3.3) for larger vibration amplitudes. A fluorescent lamp in line with the cameras is lit behind the setup for clearer visibility of vibrational amplitudes. Length of the videos varies depending on the stability of vibrations. For instance, stable vibrations occurred for electrostatic forcing and the length of the videos was 3 seconds but when the system is subjected to wind perturbations, the behaviour of the beam was random and the length of the videos captured was more than double i.e., 7 seconds. The lengths are varied to have better understanding of periodicity in the vibrations. The white vertical line in both the figures is considered to be the location of maximum displacement at the beam tip.

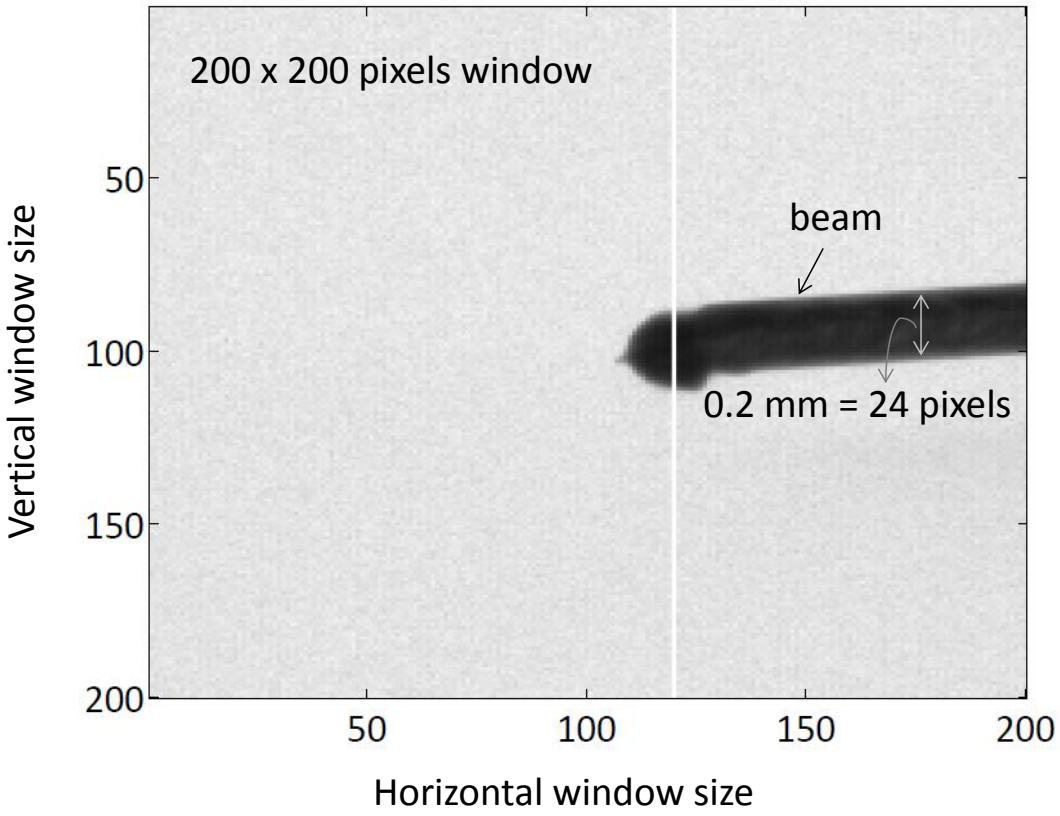

Figure 3.2: Image captured by slow camera at 250 frames per second in a 200 x 200 pixels window with a resolution of h = 0.2 mm = 24 pixels showing the location of beam tip considered for maximum displacement with white vertical line.

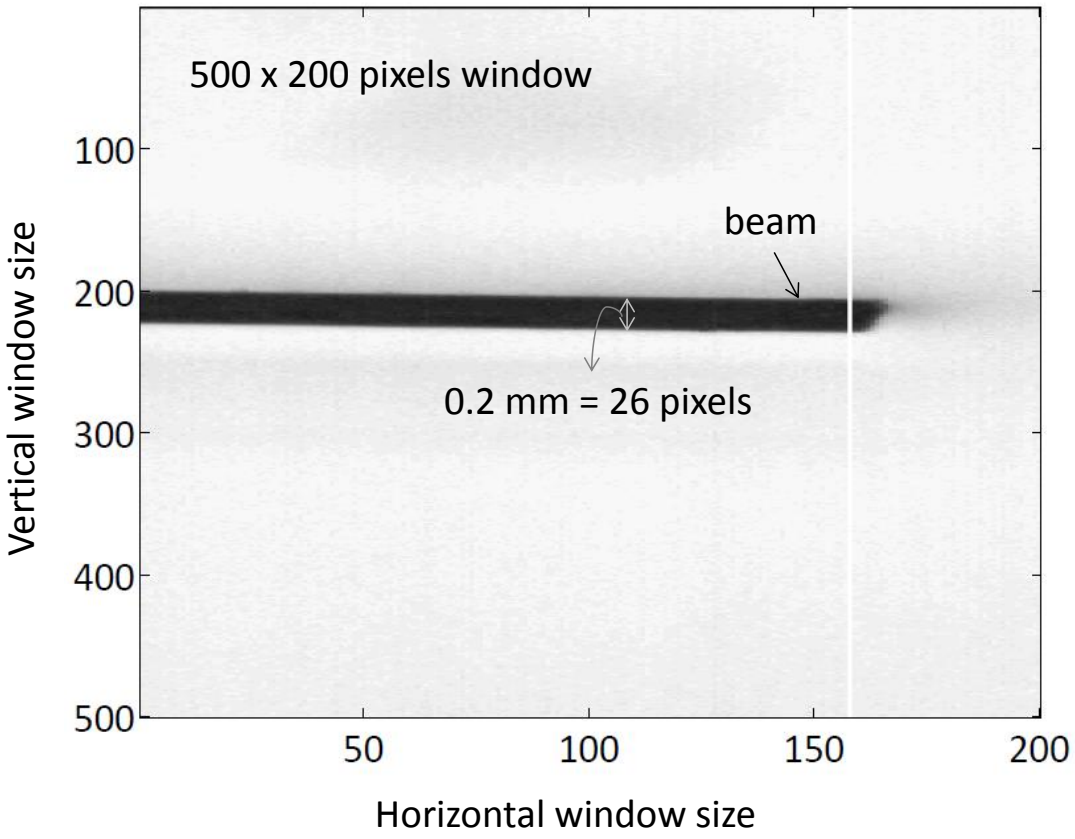

Figure 3.3: Image captured by fast camera at 1000 frames per second in a 500 x 200 pixels window with a resolution of h = 0.2 mm = 26 pixels showing the location of beam tip considered for maximum displacement with white vertical line.

3.2 Procedure

The experimental setup is used in three configurations to see the effects of the low speed air flow on electrostatic load induced vibrations of the beam. All the experiments are conducted in ambient air conditions.

Firstly, the system is excited electrostatically to measure $u_{L,e}$ by supplying DC voltage with AC modulation to the beam with the fan switched off. For this, the beam is adjusted to some gap distance 15 mm $< a_0 <$ 35 mm at 5 mm increments. The waveform generator supplies voltage ϕ_{max} on the range of 1-9 kV in 1 kV increments with one of the sine, square and triangle signals at excitation frequencies ω_ϕ ranging from 1-8 Hz in 1 Hz increments to the beam using the high voltage amplifier. The highest voltage supplied is below the breakdown voltage and this varies with the gap distance as the electric field intensity varies. Although the theoretical dielectric strength of air is 3 kV/mm, the dielectric breakdown typically occurred earlier than this value due to deflection of the electrodes. This was determined by observing an electric spark or any noise generated in the vicinity of the electrodes. For instance, at 15 mm gap distance, the dielectric breakdown should occur at 45 kV but was observed at 8 kV. This could also be the result of the shape of the electrodes which contains sharp corners, temperature, humidity and/or dust particles as mentioned in [56].

Secondly, the system is excited aerodynamically to measure $u_{L,a}$ by fixing the post at some distance and varying the air flow speeds from $U_\infty \approx 0.224$ m/s (0.5 mile/hr) to $U_\infty \approx 3.58$ m/s (8 mile/hr) in $U_\infty \approx 0.224$ m/s (0.5 mile/hr) increments with no voltage supplied. Reynolds number, Re for these speeds at the tip of the beam is found to vary as $1173 < Re < 18770$ where Re=$U_\infty x/\nu$ in which $x = 82.4\ mm$ and $\nu = 1.57\times10^{-5}\ m^2/s$ at 25 °C. Assuming the flow is steady and incompressible, similarity solution of Blasius boundary layer equation is used to determine boundary layer thickness δ on flat plate at the beam tip as $\delta = 5x/\sqrt{Re}$ which ranges from 3 mm to 12.03 mm for the calculated Re numbers.

Finally, the system is subjected to both electrostatic and aerodynamic loads to measure $u_{L,e+a}$ after determining the system stability from the first and second set of experiments. These are conducted for all gap distances with the square signal, highest voltage for a gap distance and 8 Hz excitation frequency varying the air flow speeds from $U_\infty \approx 0.224$ m/s

(0.5 mile/hr) to $U_\infty \approx 2.24$ m/s (5 mile/hr).

Experiments used to measure the elastic modulus are conducted by adjusting the beam to a specific gap distance a_0 between 15 mm and 35 mm from the ground electrode and varying steady voltage ϕ_{max} from 1-9 kV in 1 kV increments and from 9-1 kV in 1 kV decrements while recording the displacement. Three sets of this type of data are collected and averaged for each voltage. This procedure is repeated for other gap distances. Experiments used to measure the viscous damping coefficient are conducted by displacing the beam from its equilibrium position and releasing it while capturing the decaying vibrations over time.

3.3 Data Extraction

After all the required videos are captured, they are processed through a custom MATLAB code written to extract the displacement versus time data of the beam tip using the image analysis technique reading the videos frame by frame for studying the beam dynamic characteristics.

For the image analysis technique, first of all a threshold value of pixels for the beam at rest is determined by observing the pixel values of the beam tip at the location of the white line which is considered to be beam tip position. Figure 3.4 shows beam at rest with the white line which indicates that beam tip position changes along that line with time for forced loading. On the other side is a steel ruler to convert the pixels into millimeters. This ruler provides the information of the number of pixels for 1 mm, thus the scale factor to convert pixels to millimeters is determined. This scale factor is verified using the number of pixels for the beam thickness from the same image.

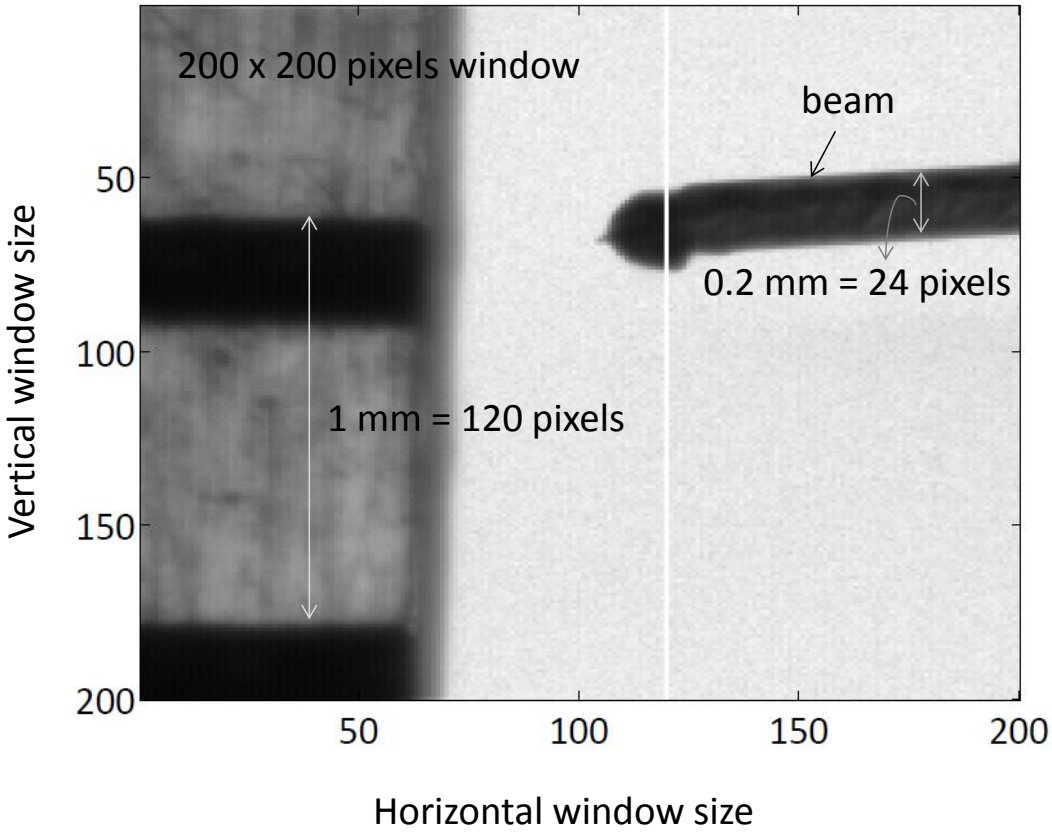

Figure 3.4: Beam at rest with the white line indicating that beam tip position changes along that line with time and pixels information to determine the scale factor to convert into millimeters.

To determine the threshold value of pixels of resting beam tip location, intensity of red color of every pixel is extracted. For the beam at rest, the intensity of red color along the white line locating the position of beam tip for every pixel along the line is determined for the vertical window size whose values range from 0 to 255, where 0 and 255 represent black and white color intensities respectively. Figure 3.5 shows the red color intensity values along the white line shown in Figure 3.4 for the vertical window size to determine the threshold value. From figures 3.4 and 3.5 the beam is located between vertical window size pixels of 55 and 75 for which the red color intensities are below 50. This value of 50 is considered

to be the threshold value to locate the position of beam tip along the white line when the beam vibrates. To find the amplitude of vibration in each frame, position of the beam tip is found. This position is obtained from the red color intensity of pixel values of the beam tip at the location of white vertical line that are below the threshold value. If the pixel values are greater than the threshold, then the location of white line moves away from the beam tip closer to the fixed end where the intensities are below threshold which gives the beam position. This is not quite the maximum tip displacement but we consider it to be maximum displacement as the white line does not move more than 5 pixels away from the considered beam tip location that results in an error of 42 μm in beam tip displacement for the less resolution slow camera. Thus the amplitude of vibration for every increase in time is determined.

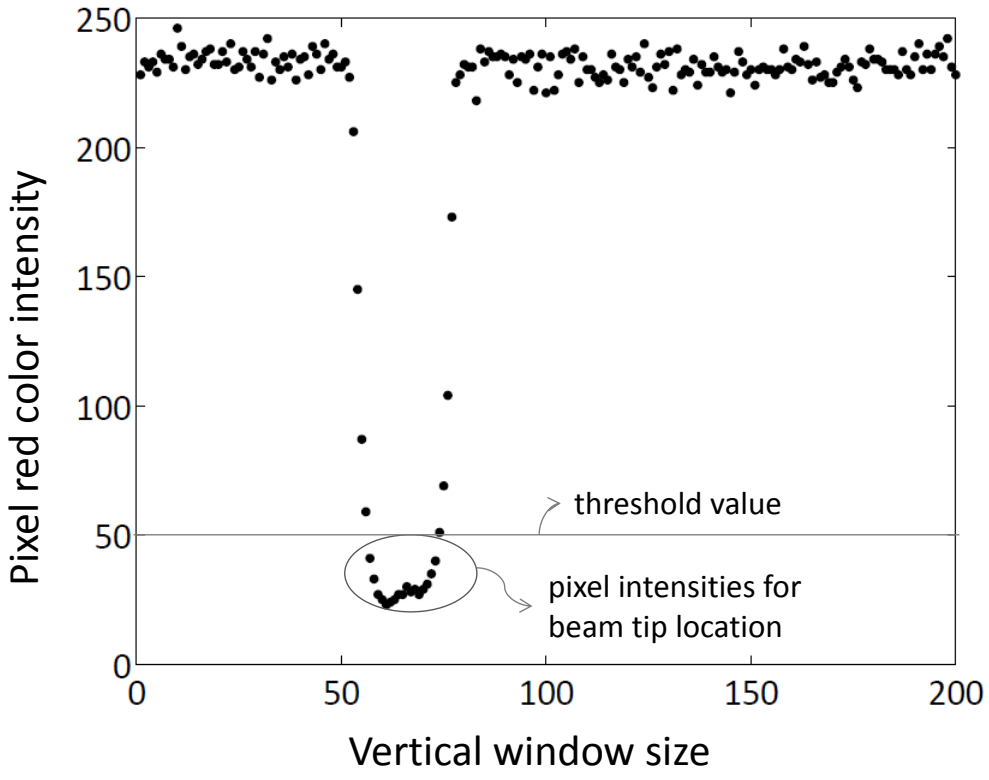

Figure 3.5: Pixel red color intensity values along the white line for the vertical window size to determine the threshold value.

CHAPTER 4. RESULTS

In order to produce accurate numerical results of non-linear, dynamic equation of motion of the beam, there is a need to estimate the elastic modulus and viscous damping coefficient of the system due to the surrounding ambient air. These are found by comparing the experimental and numerical displacements of the free end of the beam.

4.1 Elastic Modulus

Figure 4.1a shows the plot of maximum displacement due to electrostatic load at the free end, $u_{L,e}$ versus steady applied voltage, ϕ_{max} to estimate the elastic modulus of the PET film. It can be seen that as the gap distance and the applied voltage increases, the displacement decreases and increases, respectively. This is obvious from the steady electrostatic forcing term where the intensity of electrostatic force is directly proportional to ϕ_{max}^2 and inversely proportional to a_0^2. This shows that the electrostatic forces are higher at lower gap distances for the same voltage applied assisting in obtaining higher displacement amplitudes. For numerical results, Eq. 2.7 is solved as described in Sec. 2.2 to obtain the steady displacement of the beam. This plot demonstrates very good agreement between the experimental and numerical displacement curves for all the voltages applied, especially at the higher gap distances.

From the numerical data, as the gap distance decreases, displacement and the value of the elastic modulus that produces the best fit increases. The average of these values is used to estimate the elastic modulus which is 3.1 GPa. This value is reasonable based on other studies of PET films [35]. Elastic modulus may be modified to be a constant by introducing a

coefficient in electrostatic forcing term that increases with the gap distance. This coefficient has to do with the non-linearity in the equation which produces higher displacements for smaller gap distances raised to some power.

4.2 Viscous Damping Coefficient

Figure 4.1b shows the plot comparing the experimental and numerical free end underdamped vibrations of the flexible electrode over time. This plot is utilized to determine the viscous damping coefficient, C of the system. C is adjusted until the numerical vibration amplitudes are close enough to the experimental ones. For $C = 4.5 \times 10^{-4}$ N-s/m the numerical data strongly agrees with the experimental data. Additionally, from this experimental data the natural frequency of the beam, ω_n is found to be 13 Hz, after converting $u_{L,0}$ vs t data into $u_{L,0}$ vs frequency using the Fast Fourier Transform (FFT) tool in MATLAB.

After the properties of the beam and the system are known values of the four dimensionless variables are determined as $\Pi_\mu = 0.106$, $\Pi_g = 0.354$, $2.8 \times 10^{-4} \leq \Pi_a \leq 0.029$ and $4.6 \times 10^{-4} \leq \Pi_e \leq 0.122$. The range of Π_a is found using the 'k' values assumed for the aerodynamic forcing only as those values assumed for both electrostatic and aerodynamic forcing case fall in this range and of Π_e is found using steady voltage and uniform gap distance.

Now actual experiments are conducted. The same behavior like what is seen in steady load application case is noted when the dynamic voltage is applied with varying gap distance i.e. as $\phi(t)$ and a_0 increases, the amplitude of displacement increases and decreases respectively. Therefore, the results of smallest gap space $a_0 = 15$ mm and highest voltage applied $\phi_{max} = 7$ kV are considered for discussion. The influence of other variables subharmonic frequency, input signal type and air flow speed are presented below.

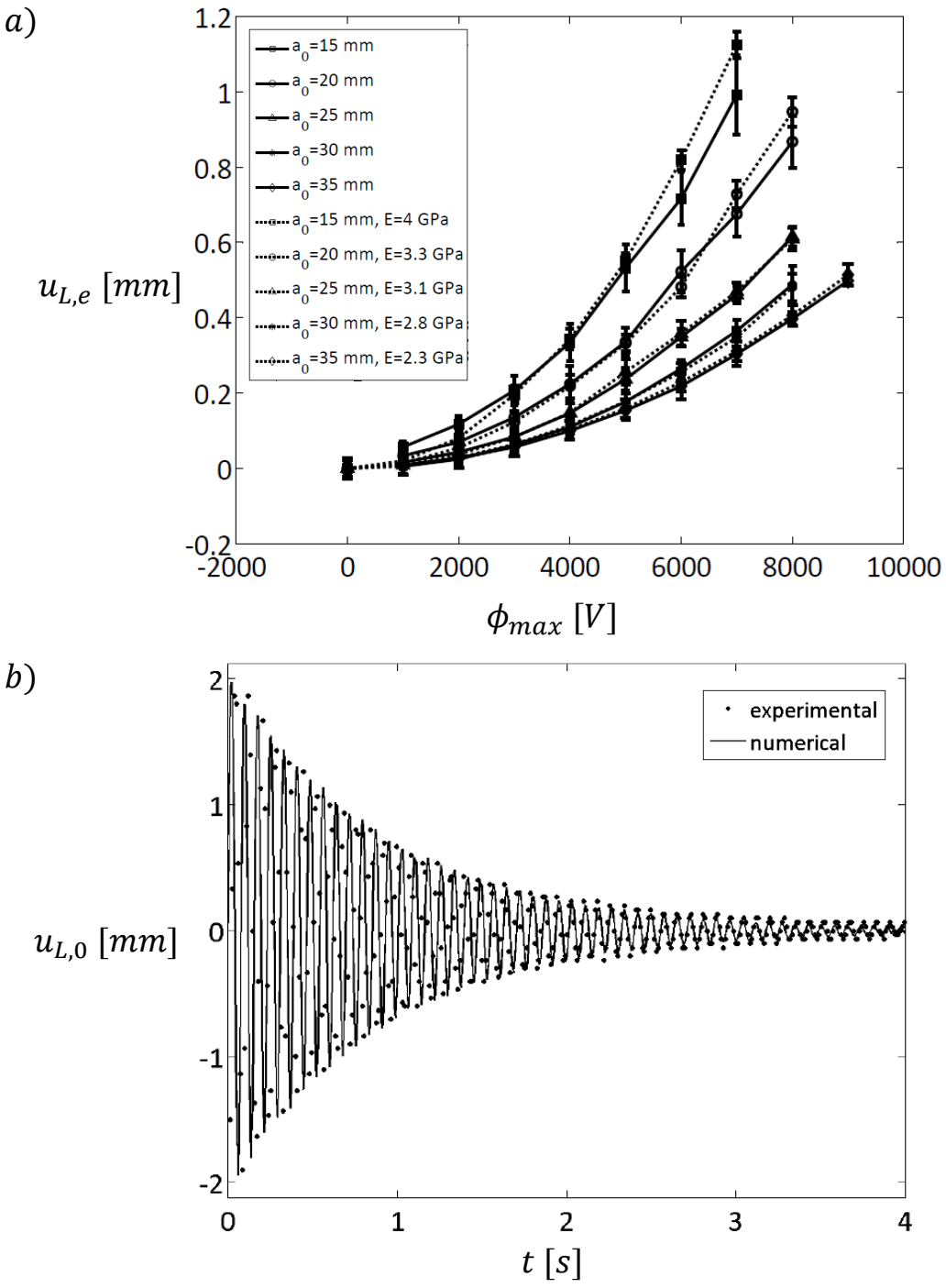

Figure 4.1: a) Comparison of experimental (solid lines) and numerical (dotted lines) maximum displacement at the free end due to electrostatic load versus steady potential applied to find elastic modulus of the beam and b) comparison of experimental (closed circles) and numerical (solid line) underdamped vibrations of the beam to find the viscous damping coefficient of the system.

4.3 Electrostatic Forcing

The beam is excited by three harmonic signals sine, square and triangle to see the impact of sinusoidal and non-sinusoidal waves with subharmonic frequencies ranging from 1 Hz to 8 Hz below the beam natural frequency (13 Hz). Zero displacement in the plots indicate equilibrium position due to gravity. Among all the frequency data sets, stable vibrations were observed when the beam is excited at 8 Hz which is probably close enough to be considered a subharmonic mode of the beam's natural frequency. Figure 4.2 shows comparison of experimental and numerical displacement time histories of free end of the beam due to electrostatic load for smallest gap distance $a_0 = 15$ mm and highest voltage applied $\phi_{max} = 7$ kV for three input signals sine, square and triangle at an excitation frequency of ω_ϕ =8 Hz. The experimental results from Figure 4.2 show that the beam exhibits similar behaviour for all the input signals i.e. the response consists of a single sine wave for one cycle of oscillation with displacement frequency equal to the excitation frequency and similar values of maximum vibration amplitudes (≈ 0.2 mm). Closer observation reveals smooth waveform in the case of a square wave input signal and lightly distorted responses in the case of sine and triangle input signals. This observation could be the result of the larger bandwidth of the square wave by the function generator which captures the subharmonic frequency of the beam nicely. Therefore it can be noted that the sine and triangle behave similarly with some instabilities while square is more stable and produces slightly higher vibration amplitudes.

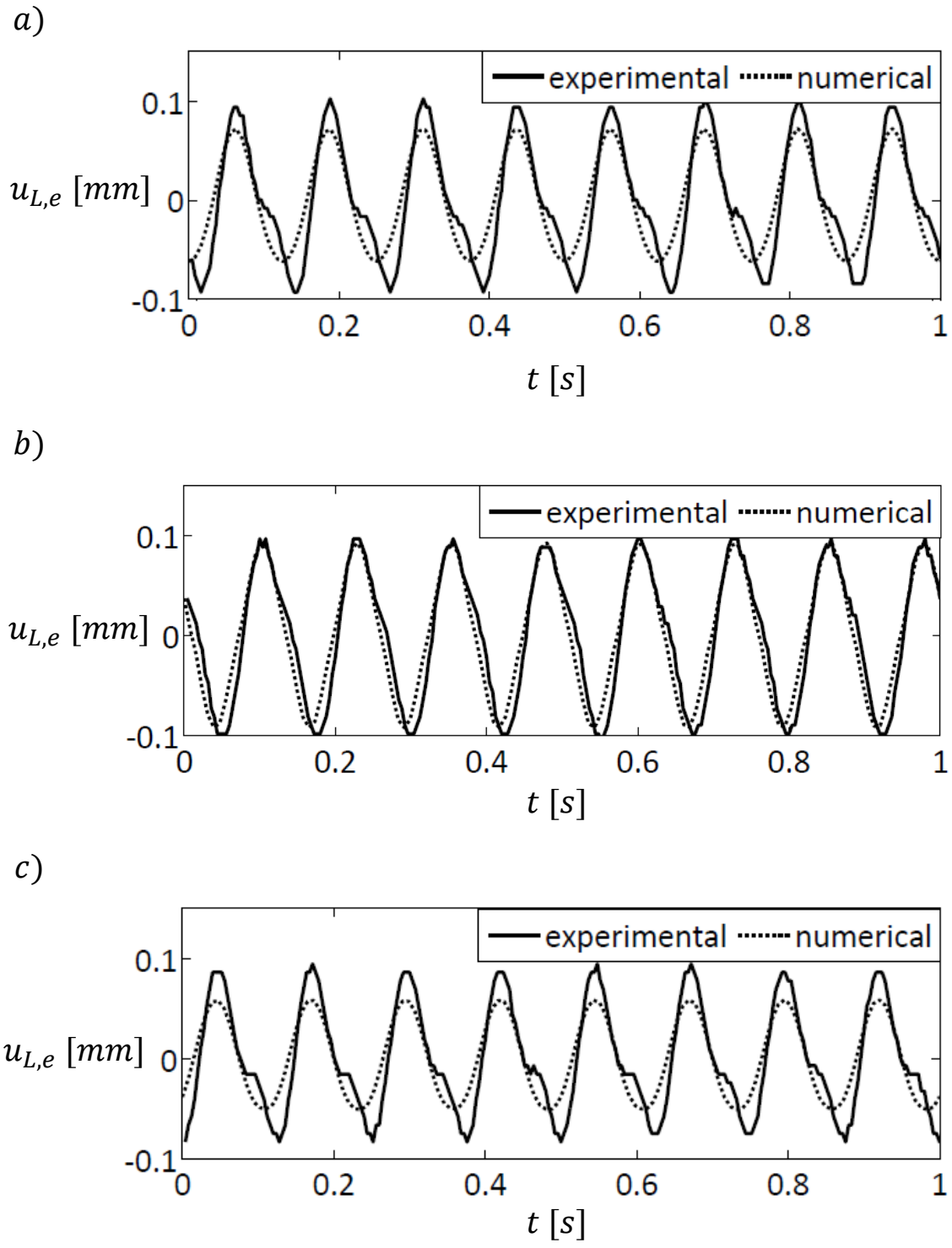

Figure 4.2: Comparison of experimental and numerical displacement time histories of free end of the beam for $a_0 = 15$ mm, $\phi_{max} = 7$ kV due to electrostatic load for three input signals a) sine, b) square and c) triangle at an excitation frequency of $\omega_\phi = 8$ Hz.

For the numerical analysis Eq. 2.2 is solved with $\Pi_a = 0$, but with a factor in the electrical forcing term which increases with the gap distance by 36 %; at lower gap distances the intensity from the electrical forcing term is considered at a minimum. These factors are determined by comparing numerical results with those of the experiments for having similar amplitudes of vibrations. The inclusion of this additional factor may be due to the non-linearity in the equation solved. This equation reproduces the response of the experimental square wave while sine and triangle responses have reduced amplitude of vibrations and much smoother behavior. Therefore we continue the discussion of the results by focusing on the square wave signal since it produces the most accurate comparison between the experimental and numerical results.

4.4 Aerodynamic Forcing and Drag Coefficient

Next we conduct experiments to study the behavior of the beam under aerodynamic forcing only. For this set of experiments we consider air flow speeds from $U_\infty \approx 0.224$ m/s (0.5 mile/hr) to $U_\infty \approx 3.58$ m/s (8 mile/hr) in $U_\infty = 0.224$ m/s (0.5 mile/hr) increments. The oscillations of flexible films under constant aerodynamic forcing occur as mentioned in [45]. From the FFT analysis of all the experimental data sets, it is observed that the displacement frequency is equal to the natural frequency of the beam until $U_\infty \approx 0.894$ m/s (2 mile/hr) after which the displacement frequency is ≈ 22 Hz. This phenomena can be understood from the experimental displacement time history results of the free end of the beam in figures 4.3a and 4.3b for $U_\infty \approx 0.894$ m/s (2 mile/hr) and $U_\infty \approx 2.24$ m/s (5 mile/hr). It is observed that the vibration amplitudes increase by $\approx 130\%$ as the speed is increased and are random for any air flow speed which can be seen in the figures. We observe that for $a_0 = 35$ mm the displacement frequency is always equal to the beams natural frequency which may indicate the presence of a small boundary layer disturbance between the vibrating beam and bottom wall (jet impingement) for $a_0 \ll 35$ mm.

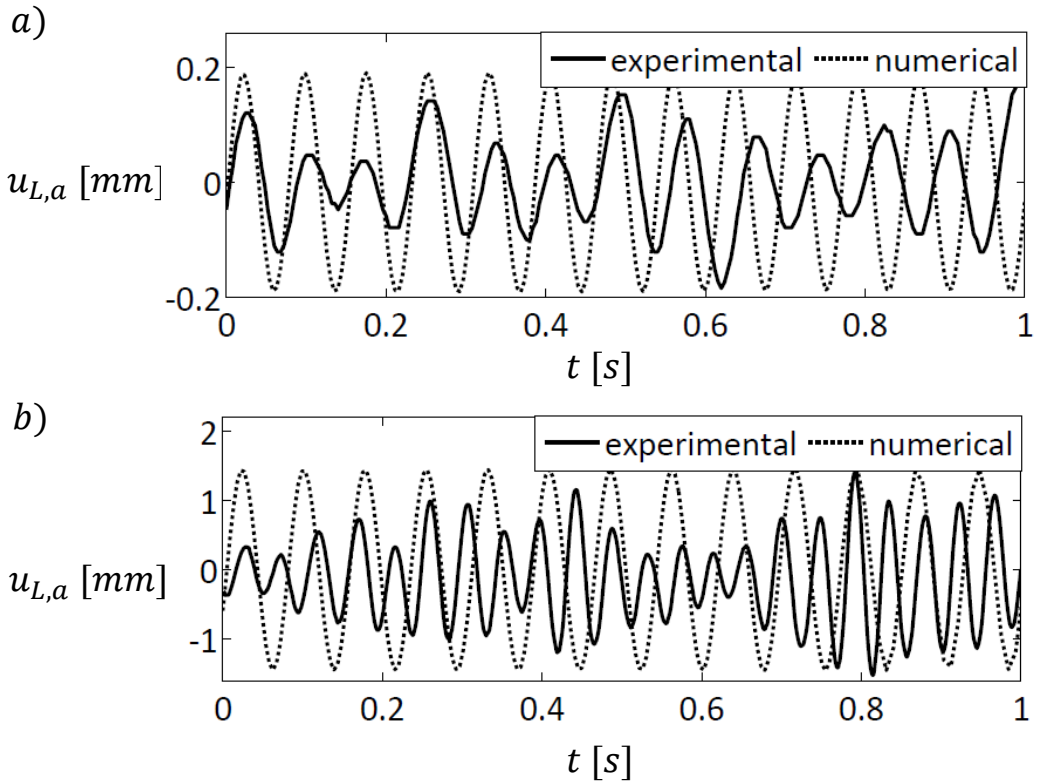

Figure 4.3: Comparison of experimental and numerical displacement time histories of free end of the beam due to aerodynamic load for $a_0 = 15$ mm with constant air flow speeds of a) $U_\infty = 0.8941$ m/s (2 mile/hr) and b) $U_\infty = 2.235$ m/s (5 mile/hr).

For the numerical analysis presented alongside the experimental data in Figure 4.3, Eq. 2.2 is solved with $\phi(t) = 0$, $\omega_n = 13$ Hz and k is set equal to the experimentally measured maximum displacement $u_{L,a}$. This reproduces the vibration amplitudes seen in the experiments but not the random behavior. The assumption that $k = u_{L,a}$ yielded numerical $u_{L,a}$ values that are only 0.1% higher than that of the experiments validating the assumption of modeling the aerodynamic forcing as a uniform sinusoidal forcing.

A drag coefficient is determined from the flow induced vibrations data. For this, as mentioned earlier k is assumed to be equal to the value of experimental free end displacement, $u_{L,a}$ for that speed and gap distance. This experimental displacement is found to be proportional to the square of the air flow velocity U_∞^2, implying the same proportionality to k i.e. $k \propto U_\infty^2$. This proportionality is then utilized to find out the drag coefficient of the

cantilever beam, $C_D = K/F_D$ where $K = kL$ and $F_D = \rho_a A U_\infty^2$ in which K is aerodynamic load applied, F_D is drag force and ρ_a is air density. Figure 4.4 shows $\ln K$ vs. $\ln F_D$ for all gap distances a_0, and air flow speeds U_∞. It can be observed that $\ln K$ increases linearly as $\ln F_D$ increases. All the data falls into the solid line except for the ones at lowest speed which may be due to 1) the low resolution of the camera to capture very small displacements and 2) the boundary effects of the ground electrode glued to the bottom acrylic plate. By interpolating linear best fit to the data, C_D is found to be 0.074. This value is in agreement with data computed for the case of plates of large aspect ratio[44].

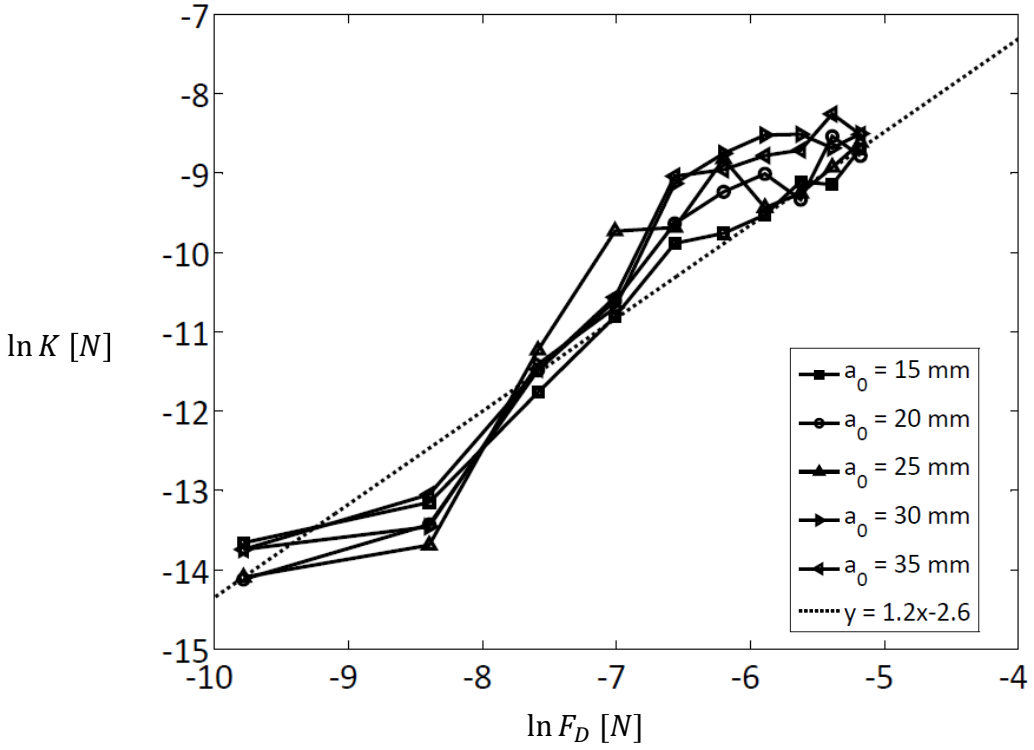

Figure 4.4: $\ln K$ Vs $\ln F_D$ for determining the drag coefficient.

4.5 Electrostatic and Aerodynamic Forcing

Low air flow speeds are selected to observe the effects of small aerodynamic forcing on stable vibrations after determining the conditions for stable vibrations of the beam under

electrical forcing and characterizing the aerodynamic forcing on the cantilever. The electrical forcing was the square input signal with 8 Hz which produced stable vibrations (see Figure 4.2b). The aerodynamic forcing was for the range of air flow speeds from $U_\infty \approx 0.224$ m/s (0.5 mile/hr) to $U_\infty \approx 2.24$ m/s (5 mile/hr). It is observed that at lower air flow speeds the amplitude of the vibration and displacement frequency are dominated by electric force corresponding to the electrical inputs giving rise to stable vibrations, where as at higher speeds the air flow controls the behavior of the beam having it excited at the natural frequency. This can be clearly seen in the experimental data of figures 4.5a and 4.5b where the displacement time history for $a_0 = 15$ mm, with square, $\phi_{max} = 7$ kV and $\omega_2 = 8$ Hz perturbed by a constant air flow speeds of $U_\infty \approx 0.224$ m/s (0.5 mile/hr) and $U_\infty \approx 2.24$ m/s (5 mile/hr) respectively are plotted.

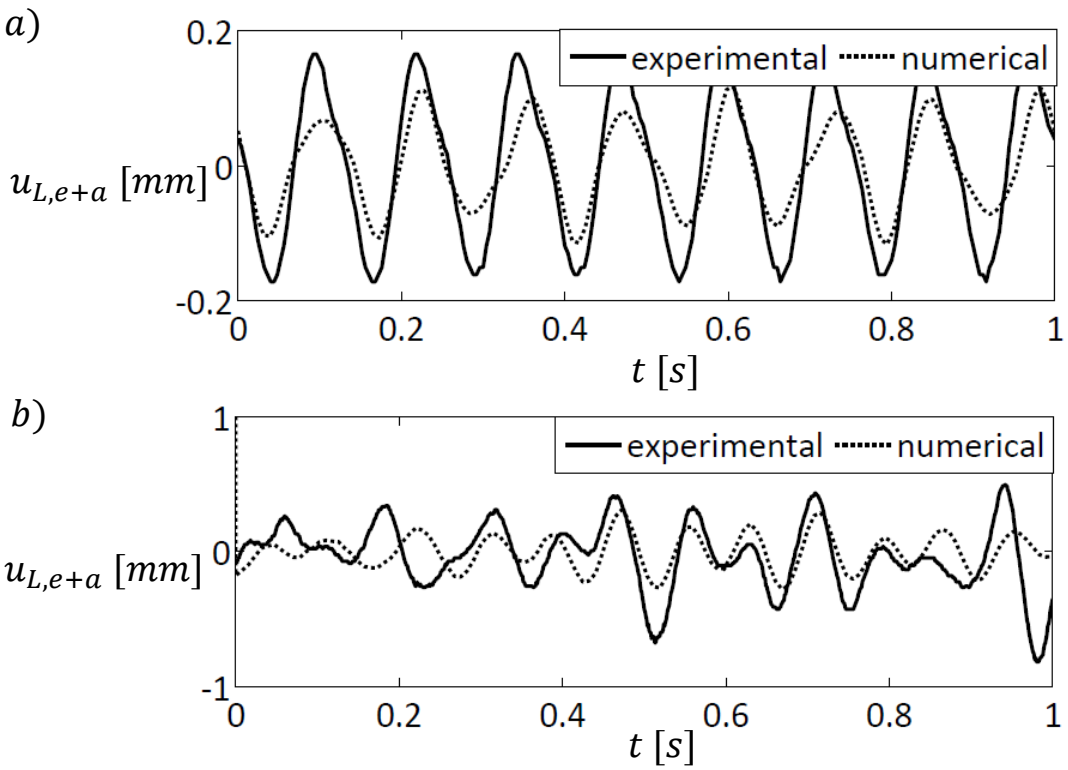

Figure 4.5: Comparison of experimental and numerical displacement time histories of free end of the beam due to electrostatic and aerodynamic loads with square, $\phi_{max} = 7$ kV, $\omega_2 = 8$ Hz, a) $U_\infty = 0.2235$ m/s (0.5 mile/hr) and b) $U_\infty = 2.235$ m/s (5 mile/hr).

For the numerical analysis Eq. 2.2 is solved with the parameters used for experiments with beam excitation at the natural frequency for aerodynamic forcing with $k \ll u_{L,e+a}$. These values of k are chosen because the frequency of the displacements correspond to the experimental ones whereas the vibration amplitudes correspond to the experimental data for $k = u_{L,e+a}$ but the output frequencies do not correspond. From Figure 4.5b, it can be seen that the numerical results strongly agree with the experimental ones producing close vibration amplitudes and apparently random behavior. These plots suggest that the amplitude of vibrations and their stability is dominated by electrostatic load at lower speeds and dominated by aerodynamic load at higher speeds and the chaotic nature increases as the air flow speed increases.

As the speed is increased the maximum vibration amplitudes increased by only $\approx 90\%$ as compared to the aerodynamic forcing data that showed an increase of 130%. It is observed that the contribution of displacement assisted by aerodynamic forcing is only 65% as compared to the case of only aerodynamic load i.e. $u_{L,e+a} = u_{L,e} + 0.65u_{L,a}$. As the gap distance increases, dominance of aerodynamic load increases exciting the beam at natural frequency at lower air flow speeds.

Phase plane diagrams are plotted to study the behavior of the beam for the combined electrostatic and aerodynamic forcing effect at lower speeds. For the experimental data, displacement versus time $u_{L,e+a}$ data extracted from MATLAB is used for x- axis and velocity versus time $v_{L,e+a}$ obtained from displacement versus time data is used for y-axis. This velocity is calculated using change in position from this position to the next position per unit time obtained from displacement versus time data. Numerical data is obtained by computing position and velocity at each time step using 4^{th} order RKM method. Figure 4.6 shows the comparison of experimental and numerical phase plane diagrams of free end of the beam

for combined electrostatic and aerodynamic forcing with square, $\phi_{max} = 7$ kV, $\omega_2 = 8$ Hz, $U_\infty = 0.2235$ m/s (0.5 mile/hr) for $a_0 = 15$ mm.

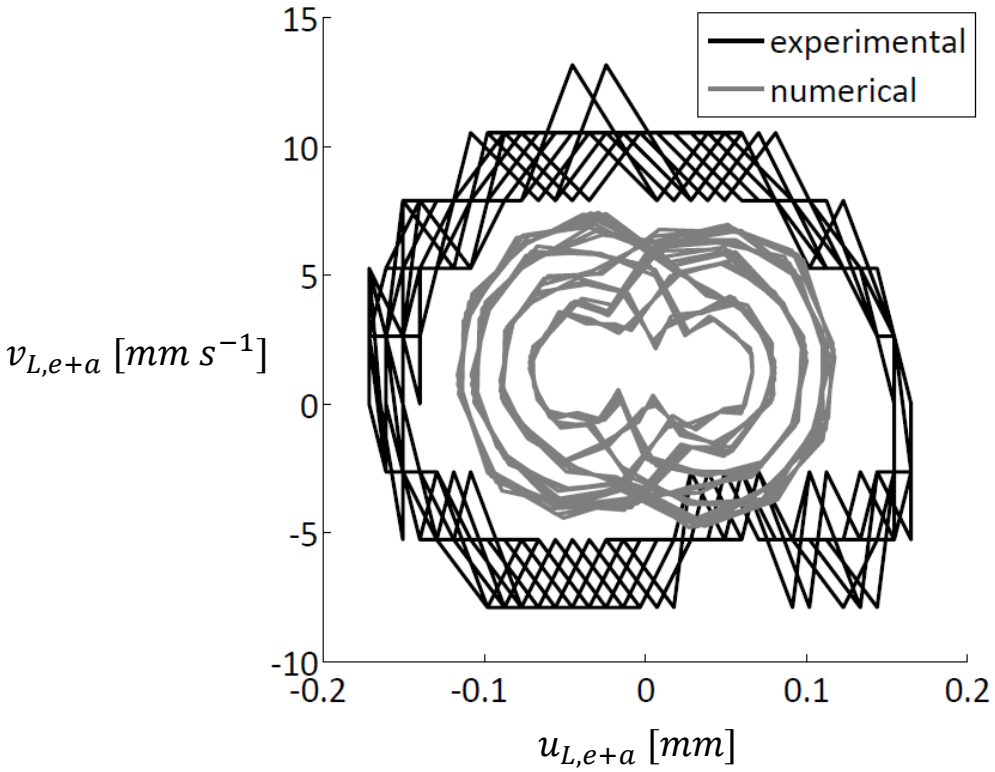

Figure 4.6: Comparison of experimental and numerical phase plane diagrams of free end of the beam due to electrostatic and aerodynamic loads with square, $\phi_{max} = 7$ kV, $\omega_2 = 8$ Hz, $U_\infty = 0.2235$ m/s (0.5 mile/hr) for $a_0 = 15$ mm.

The experimental data shows highly stable vibrations of the beam forming an ellipse. This elliptical data corresponds to that explained in [35] which is due to the dependency of electrostatic forcing on the gap distance between the electrodes. The intensity of electrostatic forcing increases with decrease in the gap distance which implies the intensity of electric field is higher at lower gap distances. As the electrostatic forcing increases depending on the input signal allowing the beam to displace toward the ground electrode, the electric field intensity increases and when the forcing is reversed, the electric field has a tendency to push the beam away quickly allowing faster rate of change in velocity which can be observed clearly at the

highest beam displacement amplitude. As the beam rises upward velocity increases slowly reaching a maximum at the zero position and then decreases slowly as the beam reaches the farthest position from the ground electrode where the electrostatic forces are minimum. Then it quickly falls down due to gravity and reaches slowly to the closest position to the ground electrode where the electrostatic forces come into play and the cycle repeats. The numerical data shows dispersed data which seems to be quasi-periodic repeating four cycles of different amplitudes over time which could be due to the two periodic forcing terms as explained in [39]. The amplitude of displacement is smaller due to considering smaller amplitude of aerodynamic forcing to obtain similar behavior of the electrode corresponding to the experiments. The phase plane diagrams at higher air flow speeds are chaotic and could not be compared to draw conclusions. Therefore St number is used to discuss the results as shown in the next section.

4.6 Discussion

In this section we discuss the results in term of the Strouhal number St in order to determine the region of stability of vibrations under electrostatic and aerodynamic forcing. For this the data of all gap distances for all air flow speeds, at the highest voltage applied for that gap distance, with square wave electrostatic forcing at $\omega_\phi = 8$ Hz is examined as shown in Figure 4.7a. Here the ratio of maximum displacement due to electrostatic and aerodynamic forcing to maximum displacement due to aerodynamic forcing $max|u_{L,e+a}|/max|u_{L,a}|$ versus $1/St$ is plotted. The data points above the $max|u_{L,e+a}|/max|u_{L,a}| = 1$ line indicate that the maximum displacement is dominated by the electrostatic load and that below the line is dominated by the aerodynamic load.

It can be observed that the ratio $max|u_{L,e+a}|/max|u_{L,a}|$ decreases as $1/St$ increases, and all the data collapses into a curve with negative slope. As we can see from the experimen-

tal data, the effect of electrostatic forcing is higher at lower $1/St$ numbers as compared to the effect of aerodynamic forcing at higher $1/St$ suggesting that aerodynamic load can be overcome effectively at lower $1/St$. As $1/St$ increases a transition from a maximum displacement dominated by electrostatic forcing to a maximum displacement dominated by aerodynamic forcing occurs. This transition is not immediate as seen in the frequency data shown in Figure 4.7b. When the displacement is dominated by electrostatic forcing, the displacement frequency is the same as excitation frequency, $\omega_\phi = 8$ Hz and when it is aerodynamically dominated the displacement frequency is close to the beams natural frequency, $\omega_n \approx 13$ Hz. In the figure, there is a region where frequencies appear at both ω_n and ω_ϕ before the transition occurs. This region increases as the a_0 increases; this can be seen as the frequency shifts from ω_ϕ to ω_n early with the increase in a_0.

While the observations of maximum displacements and frequency response to inverse Strouhal number are not surprising, the robustness of the results as measured by the single parameter for the various experimental setups are reassuring. Furthermore, the direct comparison of the numerical and experimental data for combined forcing, shown in Figure 4.5, is extremely accurate for the reduced order modelling. This is true even though the separate aerodynamic forcing only comparison shown in Figure 4.3 is not. To further explore the source of the better agreement for the combined forcing we should discuss the influence of the individual forcing terms on the resulting dynamics.

In all of the data that considers only the electrostatic forcing there is no appearance of chaotic motion as seen in the time series plots shown in Figure 4.2. We should note here that there have been some observations of chaotic motion in a similar system with a slightly longer electrode cantilever [35]. But the fact that no chaotic motion is observed for the system discussed in this paper is not necessarily surprising since chaotic motion is not seen in the forced pendulum for all forcing and damping parameters [13, 38]. Then the same reasoning

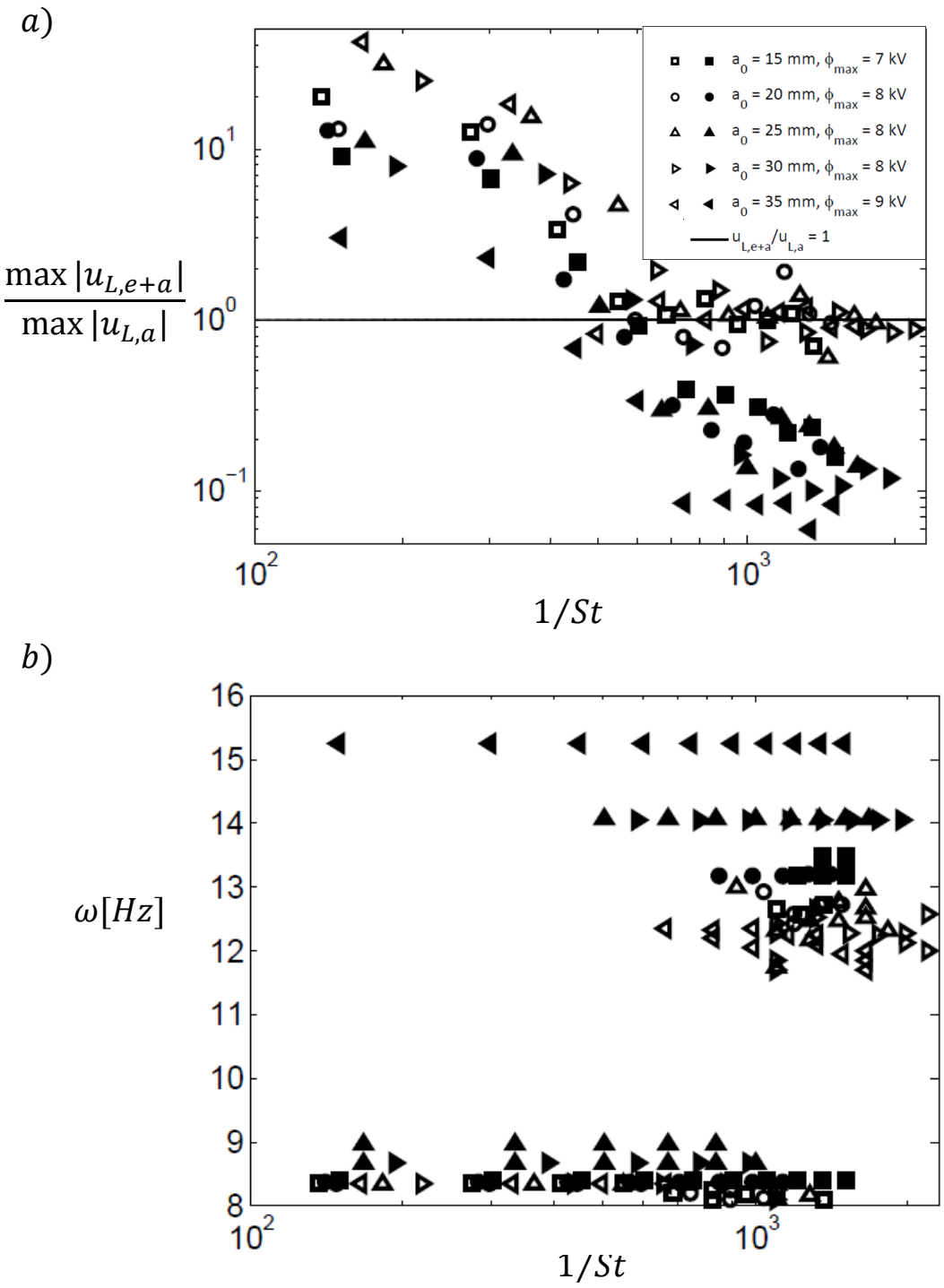

Figure 4.7: Comparison of experimental (open symbols) and numerical (closed symbols) results a) Plot of ratio of maximum displacement due to electrostatic and aerodynamic loads, $max|u_{L,e+a}|$ to maximum displacement due to aerodynamic load, $max|u_{L,a}|$ versus inverse Strouhal number, $1/St$ and b) Plot of displacement frequency versus inverse Strouhal number, $1/St$ for data analysis.

is also true for the data that only considers aerodynamic forcing since the forcing term is similar.

The lack of an appearance of random or chaotic displacements for the separate electrostatic and aerodynamic forcing would seem to suggest that the coupling of the two forcing terms is likely responsible. To understand this feature of the problem consider the appearance of additional frequencies in the coupled forcing term. To study these terms we consider a sinusoidal Λ and let $R^* \to 0$ to linearize the electrostatic forcing term. The resulting forcing term is

$$-\Pi_e f^2(x) + \Pi_a \sin y = -[\Pi_e f^2(x) + \Pi_a \sin x] + 2\Pi_a \sin\left(\frac{x+y}{2}\right)\cos\left(\frac{x-y}{2}\right) \qquad (4.1)$$

where $x = 2\pi\omega_\phi t$ and $y = 2\pi\omega_n t$. The combination of additional frequencies that are the result of the combined forcing terms and the addition of the aerodynamic term to the electrostatic forcing are clearly responsible for the agreement seen between experiments and numerical results figures 4.5b and 4.6. This suggest that the coupled system is not chaotic but quasi-periodic [40].

The result though does not conclusively determine the response seen in the data that only considers the aerodynamic forcing i.e. it may still be chaotic. Although one possible process for developing a model to test this hypothesis could be formulated by adding multiple periodic forcing terms to model the aerodynamic loading. If the terms have similar frequency but varying amplitude then this would also probably improve the agreement. In particular this may explain the results shown in Figure 4.7b where frequencies slightly higher than the natural one begin to appear. Although the underlying system is non-linear so these frequencies may appear by adding non-linear terms [57].

CHAPTER 5. CONCLUSIONS

The dynamic characteristics of an electrostatically actuated thin flexible electrode cantilever under low-speed air flow perturbations were studied experimentally and numerically. A model was developed based on Euler-Bernoulli beam theory. Static non-linear and dynamic linear Euler-Bernoulli equations were solved to estimate the elastic modulus and natural frequency of the beam and viscous damping coefficient of the system respectively by comparing those solutions with experimental results. Both static and periodic forcing results show that as the applied voltage and the gap distances were increased, the amplitude of the electrode cantilever displacement increased and decreased, respectively. Forced harmonic electrostatic excitation of the beam produced stable vibrations at 8 Hz for square wave input signal which are reproduced by the dynamic non-linear Euler-Bernoulli equation. Similar vibrational amplitudes are obtained by having magnitude of electrical force in this equation increase as the gap space increases.

As the system is subjected to small aerodynamic loads, undisturbed higher vibrational amplitudes (as compared to electrostatic forcing data) are obtained for air flow speeds $<$ 0.447 m/s (1 mile/hour) corresponding to the electric input variables. But as the air flow speed increases, the vibrations become unstable, vibrating at beam's natural frequency with reduced amplitude of vibrations (as compared to aerodynamic forcing data). Modelling the aerodynamic forcing as single periodic term produces poor agreement with experimental observations when no electrostatic forcing is included. But including the combination of both electrostatic and aerodynamic forcing in the equation of motion not only predicted the behavior of the beam but also produced similar vibrational amplitudes at higher air flow speeds

validating the assumption.

A comparison between the experimental and numerical data is made using the Strouhal number. Here, it is defined as the ratio of the flexible electrode cantilever's vertical velocity and the free stream velocity. Using the subharmonic frequency of the electrostatic forcing it is possible to determine which forcing mechanism, either electrostatic or aerodynamic, is mostly responsible for the cantilever tips displacement and response frequency. Direct comparisons of waveform data are also made between the experimental and numerical results with fairly good agreement.

In the future, aerodynamic forcing can be modified as a non-linear term including more periodic forcing terms of same amplitude or method of slowly varying amplitude and phase as described in [58] to account for the random behavior seen in the experiments. Experimental observations with electrostatic forcing at beam natural frequency could provide more insight into studying the random behavior and lifting case of the flexible beam under combined forcing conditions. Studying the behaviour of beam with different elasticities and complex geometries could lead to developing better MAV configurations. Studies with other orientations of the film with respect to air flow direction could lead to better understanding of control strategies. Extending the study to other degrees of freedom would be useful in establishing accurate control parameters range for the system.

BIBLIOGRAPHY

[1] P. B. S. Lissaman. Low-reynolds-number airfoils. *Annual Review of Fluid Mechanics*, 15(1):223–239, 1983.

[2] G. R. Spedding. The aerodynamics of flight. *Mechanics of Animal Locomotion*, 11: 52–111, 1992.

[3] C. P. Ellington. The novel aerodynamics of insect flight: applications to micro-air vehicles. *Journal of Experimental Biology*, 202(23):3439–3448, 1999.

[4] J. M. Wakeling and C. P. Ellington. Dragonfly flight. ii. velocities, accelerations and kinematics of flapping flight. *Journal of Experimental Biology*, 200(3):557–582, 1997.

[5] A. P. Willmott and C. P. Ellington. The mechanics of flight in the hawkmoth manduca sexta. ii. aerodynamic consequences of kinematic and morphological variation. *Journal of Experimental Biology*, 200(21):2723–2745, 1997.

[6] S. N. Fry, R. Sayaman, and M. H. Dickinson. The aerodynamics of hovering flight in drosophila. *Journal of Experimental Biology*, 208(12):2303–2318, 2005.

[7] T. L. Hedrick, B. Cheng, and X. Deng. Wingbeat time and the scaling of passive rotational damping in flapping flight. *Science*, 324(5924):252–255, 2009.

[8] M. F. M. Osborne. Aerodynamics of flapping flight with application to insects. *Journal of Experimental Biology*, 28(2):221–245, 1951.

[9] S. P. Sane. The aerodynamics of insect flight. *Journal of Experimental Biology*, 206 (23):4191–4208, 2003.

[10] S. R. Jongerius and D. Lentink. Structural analysis of a dragonfly wing. *Experimental Mechanics*, 50(9):1323–1334, 2010.

[11] J. M. V. Rayner. Vertebrate flapping flight mechanics and aerodynamics, and the evolution of flight in bats. *Biona Report*, 5:27–74, 1986.

[12] M. I. Woods, J. F. Henderson, and G. D. Lock. Energy requirements for the flight of micro air vehicles. *Aeronautical Journal*, 105(1045):135–149, 2001.

[13] E. G. Gwinn and R. M. Westervelt. Intermittent chaos and low-frequency noise in the driven damped pendulum. *Physical Review Letters*, 54(15):1613, 1985.

[14] R. J. Wood. The first takeoff of a biologically inspired at-scale robotic insect. *Robotics, IEEE Transactions On*, 24(2):341–347, 2008.

[15] K. Y. Ma, P. Chirarattananon, S. B. Fuller, and R. J. Wood. Controlled flight of a biologically inspired, insect-scale robot. *Science*, 340(6132):603–607, 2013.

[16] M. Keennon, K. Klingebiel, H. Won, and A. Andriukov. Development of the nano hummingbird: A tailless flapping wing micro air vehicle. In *50th AIAA Aerospace Sciences Meeting Including the New Horizons Forum and Aerospace Exposition, Nashville, TN. January*, pages 9–12, 2012.

[17] J. D. Jackson and J. D. Jackson. *Classical electrodynamics*, volume 3. Wiley New York etc., 1962.

[18] D. J. Griffiths and R. College. *Introduction to electrodynamics*, volume 3. prentice Hall Upper Saddle River, NJ, 1999.

[19] T. Gotszalk, P. Grabiec, and I. W. Rangelow. Piezoresistive sensors for scanning probe microscopy. *Ultramicroscopy*, 82(1):39–48, 2000.

[20] G. R. Spedding and P. B. S. Lissaman. Technical aspects of microscale flight systems. *Journal of Avian Biology*, pages 458–468, 1998.

[21] T. J. Mueller. *Fixed and flapping wing aerodynamics for micro air vehicle applications*, volume 195. AIAA, 2001.

[22] R. Madangopal, Z. A. Khan, and S. K. Agrawal. Biologically inspired design of small flapping wing air vehicles using four-bar mechanisms and quasi-steady aerodynamics. *Journal of Mechanical Design*, 127(4):809–816, 2005.

[23] J. Yan, R. J. Wood, S. Avadhanula, M. Sitti, and R. S. Fearing. Towards flapping wing control for a micromechanical flying insect. In *Robotics and Automation, 2001. Proceedings 2001 ICRA. IEEE International Conference on*, volume 4, pages 3901–3908. IEEE, 2001.

[24] M. J. C. Smith. Simulating moth wing aerodynamics-towards the development of flapping-wing technology. *AIAA Journal*, 34(7):1348–1355, 1996.

[25] D. L. Raney and E. C. Slominski. Mechanization and control concepts for biologically inspired micro air vehicles. *Journal of Aircraft*, 41(6):1257–1265, 2004.

[26] S. Ho, H. Nassef, N. Pornsinsirirak, Y. C. Tai, and C. M. Ho. Unsteady aerodynamics and flow control for flapping wing flyers. *Progress in Aerospace Sciences*, 39(8):635–681, 2003.

[27] R. J Wood, B. Finio, M. Karpelson, K. Ma, N. O. Pérez-Arancibia, P. S. Sreetharan, H. Tanaka, and J. P. Whitney. Progress on 'pico'air vehicles. *International Journal of Robotics Research*, 31(11):1292–1302, 2012.

[28] G. Rezazadeh, M. Fathalilou, R. Shabani, S. Tarverdilou, and S. Talebian. Dynamic characteristics and forced response of an electrostatically-actuated microbeam subjected to fluid loading. *Microsystem Technologies*, 15(9):1355–1363, 2009.

[29] Y. C. Hu, C. M. Chang, and S. C. Huang. Some design considerations on the electrostatically actuated microstructures. *Sensors and Actuators A: Physical*, 112(1):155–161, 2004.

[30] E. M. Abdel-Rahman, M. I Younis, and A. H. Nayfeh. Characterization of the mechanical behavior of an electrically actuated microbeam. *Journal of Micromechanics and Microengineering*, 12(6):759, 2002.

[31] S. Chaterjee and G. Pohit. A large deflection model for the pull-in analysis of electrostatically actuated microcantilever beams. *Journal of Sound and Vibration*, 322(4): 969–986, 2009.

[32] S. Pamidighantam, R. Puers, K. Baert, and H. A. C. Tilmans. Pull-in voltage analysis of electrostatically actuated beam structures with fixed–fixed and fixed–free end conditions. *Journal of Micromechanics and Microengineering*, 12(4):458, 2002.

[33] S. Krylov and R. Maimon. Pull-in dynamics of an elastic beam actuated by continuously distributed electrostatic force. *Journal of Vibration and Acoustics*, 126(3):332–342, 2004.

[34] S. Chowdhury, M. Ahmadi, and W. C. Miller. A closed-form model for the pull-in voltage of electrostatically actuated cantilever beams. *Journal of Micromechanics and Microengineering*, 15(4):756, 2005.

[35] C. D. Hinton. Investigation of stability in an electrostatically actuated film. Master's thesis, North Carolina State University, 2012.

[36] R. Shabani, H. Hatami, F. G. Golzar, S. Tariverdilo, and G. Rezazadeh. Coupled vibration of a cantilever micro-beam submerged in a bounded incompressible fluid domain. *Acta Mechanica*, 224(4):841–850, 2013.

[37] W. E. Baker, W. E. Woolam, and D. Young. Air and internal damping of thin cantilever beams. *International Journal of Mechanical Sciences*, 9(11):743–766, 1967.

[38] G. L. Baker and J. P. Gollub. *Chaotic dynamics: an introduction*. Cambridge University Press, 1996.

[39] F. J. Romeiras and E. Ott. Strange nonchaotic attractors of the damped pendulum with quasiperiodic forcing. *Physical Review A*, 35(10):4404, 1987.

[40] F. J. Romeiras, A. Bondeson, E. Ott, T. M. Antonsen, and C. Grebogi. Quasiperiodically forced dynamical systems with strange nonchaotic attractors. *Physica D: Nonlinear Phenomena*, 26(1):277–294, 1987.

[41] W. L. Ditto, M. L. Spano, H. T. Savage, S. N. Rauseo, J. Heagy, and E. Ott. Experimental observation of a strange nonchaotic attractor. *Physical Review Letters*, 65(5): 533, 1990.

[42] F. D. Bona and E. T. Enikov. *Microsystems mechanical design*, volume 478. Springer Science & Business Media, 2006.

[43] N. Sharafkhani, R. Shabani, S. Tariverdilo, and G. Rezazadeh. Stability analysis and transient response of electrostatically actuated microbeam interacting with bounded compressible fluids. *Journal of Applied Mechanics*, 80(1):011024, 2013.

[44] D. L. A. Lisoski. *Nominally 2-dimensional flow about a normal flat plate*. PhD thesis, California Institute of Technology, 1993.

[45] M. Glück, M. Breuer, F. Durst, A. Halfmann, and E. Rank. Computation of wind-induced vibrations of flexible shells and membranous structures. *Journal of Fluids and Structures*, 17(5):739–765, 2003.

[46] K. M. Lam and M. Y. H. Leung. Asymmetric vortex shedding flow past an inclined flat plate at high incidence. *European Journal of Mechanics-B/Fluids*, 24(1):33–48, 2005.

[47] L. Wang, Y. Wang, and Z. Li. A method to estimate vortex shedding frequency in turbulence. In *Image and Signal Processing (CISP), 2010 3rd International Congress on*, volume 7, pages 3386–3390. IEEE, 2010.

[48] S. K. De and N. R. Aluru. Complex nonlinear oscillations in electrostatically actuated microstructures. *Journal of Microelectromechanical Systems*, 15(2):355–369, 2006.

[49] J. T. Libo-on, J. E. C. Lope, and R. C. H. Del Rosario. Heuristic methods for parameter estimation in a smart beam structure. In *Proceedings of the World Congress on Engineering*, volume 2, 2008.

[50] G. Piccardo and F. Tubino. Dynamic response of euler-bernoulli beams to resonant harmonic moving loads. *Structural Engineering and Mechanics*, 44(5):681–704, 2012.

[51] M. S. Triantafyllou and G. S. Triantafyllou. An efficient swimming machine. *Scientific American*, 272(3):64–71, 1995.

[52] G. K. Taylor, R. L. Nudds, and A. L. R. Thomas. Flying and swimming animals cruise at a strouhal number tuned for high power efficiency. *Nature*, 425(6959):707–711, 2003.

[53] M. F. Platzer, K. D. Jones, J. Young, and J. C. S. Lai. Flapping wing aerodynamics: progress and challenges. *AIAA Journal*, 46(9):2136–2149, 2008.

[54] H. Hu, A. G. Kumar, G. Abate, and R. Albertani. An experimental investigation on the aerodynamic performances of flexible membrane wings in flapping flight. *Aerospace Science and Technology*, 14(8):575–586, 2010.

[55] J. H. Ferziger. *Numerical methods for engineering application*, volume 1. Wiley New York, 1981.

[56] P. B. Sankar. *Measurement of air breakdown voltage and electric field using standad sphere gap method*. PhD thesis, National Institute of Technology, Rourkela, 2011.

[57] R. F. A. Castro, L. Guillamot, A. Cros, and C. Eloy. Non-linear effects on the resonant frequencies of a cantilevered plate. *Journal of Fluids and Structures*, 46:165–173, 2014.

[58] L. D. Lutes and S. Sarkani. *Random vibrations: analysis of structural and mechanical systems*. Butterworth-Heinemann, 2004.